The spin of the black hole microquasar XTE J1550–564 via the continuum-fitting and Fe-line methods

Monthly Notices
of the
ROYAL ASTRONOMICAL SOCIETY

Mon. Not. R. Astron. Soc. **416,** 941–958 (2011) doi:10.1111/j.1365-2966.2011.19089.x

The spin of the black hole microquasar XTE J1550−564 via the continuum-fitting and Fe-line methods

James F. Steiner,[1⋆] Rubens C. Reis,[2⋆] Jeffrey E. McClintock,[1] Ramesh Narayan,[1] Ronald A. Remillard,[3] Jerome A. Orosz,[4] Lijun Gou,[1] Andrew C. Fabian[2] and Manuel A. P. Torres[1,5]

[1]*Harvard–Smithsonian Center for Astrophysics, 60 Garden Street, Cambridge, MA 02138, USA*
[2]*Institute of Astronomy, Cambridge University, Madingley Road, Cambridge CB3 0HA*
[3]*MIT Kavli Institute for Astrophysics and Space Research, MIT, 70 Vassar Street, Cambridge, MA 02139, USA*
[4]*Department of Astronomy, San Diego State University, 5500 Campanile Drive, San Diego, CA 92182-1221, USA*
[5]*SRON, Netherlands Institute for Space Research, Sorbonnelaan 2, 3584 CA Utrecht, the Netherlands*

Accepted 2011 May 17. Received 2011 May 14; in original form 2010 October 4

ABSTRACT

We measure the spin of XTE J1550−564 using the two leading methods: (i) modelling the thermal continuum spectrum of the accretion disc; and (ii) modelling the broad red wing of the reflection fluorescence Fe Kα line. We find that these two independent measurements of spin are in agreement. For the continuum-fitting analysis, we use a data sample consisting of several dozen *Rossi X-ray Timing Explorer* spectra, and for the Fe Kα analysis, we use a pair of *ASCA* spectra from a single epoch. Our spin estimate for the black hole primary using the continuum-fitting method is $-0.11 < a_* < 0.71$ (90 per cent confidence), with a most likely spin of $a_* = 0.34$. In obtaining this result, we have thoroughly explored the dependence of the spin value on a wide range of model-dependent systematic errors and observational errors; our precision is limited by uncertainties in the distance and orbital inclination of the system. For the Fe-line method, our estimate of spin is $a_* = 0.55^{+0.15}_{-0.22}$. Combining these results, we conclude that the spin of this black hole is moderate, $a_* = 0.49^{+0.13}_{-0.20}$, which suggests that the jet activity of this microquasar is powered largely by its accretion disc rather than by the spin energy of the black hole.

Key words: accretion, accretion discs – black hole physics – stars: individual: XTE J1550−564 – X-rays: binaries.

1 INTRODUCTION

During its principal 1998–99 outburst cycle, the bright X-ray transient XTE J1550−564 produced one of the most remarkable flare events ever observed for a black hole (BH) binary. For ≈1 day, the source intensity rose four-fold relative to neighbouring plateau values, reaching 6.8 Crab. The flux in the dominant power-law component rose by the same factor and then just as quickly its intensity declined (Sobczak et al. 2000; McClintock et al. 2009). 4 days later, au-scale superluminal radio jets were observed (Hannikainen et al. 2009). Their separation angle (∼255 mas) and relative velocity (∼65 mas d^{-1}) link the birth of these jets to the impulsive X-ray flare. The subsequent detection of large-scale radio jets in 2000 led to the discovery of relativistic X-ray jets (Corbel et al. 2002; Kaaret et al. 2003; Tomsick et al. 2003). All of the available evidence strongly indicates that these pc-scale X-ray and radio jets were produced during the unique 7-Crab flare event, and we adopt this view.

The microquasar XTE J1550−564 (hereinafter J1550) is further distinguished by a pair of high-frequency X-ray oscillations with a 2:3 frequency ratio (184 and 276 Hz; Miller et al. 2001; Remillard et al. 2002a). During its 1998–99 eruption, J1550 displayed all of the active accretion states: hard, steep power law (SPL), thermal dominant (TD) and intermediate (INT; Remillard & McClintock 2006). The X-ray spectral and timing properties of this source have been comprehensively studied by many authors (e.g. Sobczak et al. 2000; Homan et al. 2001; Remillard et al. 2002b; Kubota & Done 2004; Dunn et al. 2010), as have been the properties of its radio counterpart (Corbel et al. 2001; Xue, Wu & Cui 2008; Hannikainen et al. 2009).

Likewise, the optical counterpart of J1550 was the subject of a comprehensive dynamical study by Orosz et al. (2002). The

⋆E-mail: jsteiner@cfa.harvard.edu (JFS); rcr36@ast.cam.ac.uk (RCR)

measurement by these authors of a large mass function immediately established J1550 as a dynamically confirmed BH binary with a $\approx 10\,M_\odot$ BH primary in a 1.55-d orbit with a late-G or early-K companion. This dynamical model was recently revisited using new photometric and spectroscopic data (Orosz et al. 2011). Our higher resolution spectra ($60\,km\,s^{-1}$) revealed that the mass ratio is extreme ($Q \approx 30$) and yielded a refined value of the mass function, $f(M) = 7.65 \pm 0.38\,M_\odot$. Of central importance to this paper, Orosz et al. (2011) report accurate values of the three key quantities that are essential for determining the spin of the BH via the continuum-fitting (CF) method, namely the distance $D = 4.38^{+0.58}_{-0.41}$ kpc, BH mass $M = 9.10 \pm 0.61\,M_\odot$ and orbital inclination angle $i = 74.^\circ7 \pm 3.^\circ8$.

Currently, the two principal methods for measuring BH spin[1] are modelling the thermal spectrum of the accretion disc (Zhang, Cui & Chen 1997) and modelling the profile of the Fe Kα line (Fabian et al. 1989; Laor 1991). For both methods, spin is measured by estimating the inner radius of the accretion disc, $r_{in} \equiv R_{in}/M$, in standard general relativistic (GR) units ($G = c = 1$). R_{in} is identified with the radius of the innermost stable circular orbit (ISCO), R_{ISCO}, about the BH and is related to spin via a monotonic mapping between the dimensionless ISCO radius, R_{ISCO}/M, and the dimensionless spin parameter a_* (Shapiro & Teukolsky 1983). Strong support for linking R_{in} to R_{ISCO} is provided by decades of empirical evidence that r_{in} is constant in disc-dominated states of BH binaries (e.g. Tanaka & Lewin 1995; Done, Gierliński, Kubota 2007). This is shown most compellingly in our recent study of the persistent source LMC X−3 (Steiner et al. 2010). Theoretical support for identifying R_{in} with R_{ISCO} is provided by magnetohydrodynamic simulations of thin accretion discs (Reynolds & Fabian 2008; Shafee et al. 2008; Penna et al. 2010; Kulkarni et al. 2011; but see Noble, Krolik & Hawley 2009, 2010). In short, the relationship for thin accretion discs between r_{in}, R_{ISCO} and a_* is the foundation of both the CF and Fe Kα methods of measuring spin.

In the CF method, one determines R_{ISCO}, and thereby a_*, via measurements of X-ray temperature and luminosity (i.e. using X-ray flux, distance D and inclination angle i) of the disc emission. In order to obtain reliable values of a_*, it is essential to (1) select X-ray spectra that have a strong thermal component, and (2) have accurate estimates of D, M and i, like those given above for J1550. In practice, we fit the X-ray spectrum of the BH's accretion disc to our version of the Novikov–Thorne thin accretion disc model (Novikov & Thorne 1973; Li et al. 2005; McClintock et al. 2006) using an advanced treatment of spectral hardening (Davis et al. 2005; Davis & Hubeny 2006). In this way, we have measured the spin values of six other stellar BHs. We find spin values ranging from $a_* \approx 0.1$ (Gou et al. 2010) to $a_* > 0.98$ (McClintock et al. 2006); four other spin values are relatively high, $a_* \approx 0.7$–0.9 (Shafee et al. 2006; Liu et al. 2008, 2010; Gou et al. 2009).

In the Fe Kα method, one determines R_{ISCO} by modelling the profile of reflection-fluorescent features in the disc. Most prominent is the broad and asymmetric iron line, whose shape is determined by Doppler effects, light bending and gravitational redshift (Reynolds & Nowak 2003). Of central importance is the effect of the redshift on the red wing of the line. This wing extends to very low energies for a rapidly rotating BH ($a_* \sim 1$) because in this case gas can orbit near the event horizon, deep in the potential well of the BH. Relative to the CF method, measuring the extent of this red wing in order to infer a_* is hindered by the relative faintness of the signal. However, the Fe Kα method has the virtue that it is independent of M and D, while the blue wing of the line even allows an estimate of i. What makes the Fe Kα method enormously important is that it is the primary approach for measuring the spin values of supermassive BHs in active galactic nuclei (AGNs). The spin values of several stellar BHs (Blum et al. 2009; Miller et al. 2009b; Reis et al. 2009, 2011) and supermassive BHs (Brenneman & Reynolds 2006; Fabian et al. 2009; Miniutti et al. 2009; Schmoll et al. 2009; Zoghbi et al. 2010) have been reported using the Fe-line method with values ranging from $a_* \approx 0$ to $a_* > 0.98$.

Knowledge of BH spin has broad importance in astrophysics; for example, spin is central to most of the many theories of relativistic jets observed for both microquasars and AGNs (Blandford & Znajek 1977, hereinafter BZ), and it is comparably important to collapsar models of long gamma-ray bursts (GRBs; Woosley 1993) and models of BH formation and BH binary evolution (Lee, Brown & Wijers 2002). Hierarchical models for the growth of supermassive BHs require knowledge of the spin distributions of the merging partners (Volonteri et al. 2005; Berti & Volonteri 2008), and the observed properties of AGNs may be strongly conditioned by BH spin (McNamara et al. 2009; Garofalo, Evans & Sambruna 2010; Tchekhovskoy, Narayan & McKinney 2010). Spin measurements are likewise important to gravitational wave astronomy in predicting the waveforms of merging BHs (Campanelli, Lousto & Zlochower 2006). Knowledge of BH spin is becoming important to fundamental physics as well, and enlivening questions are being asked, for example, is the no-hair theorem valid and can it be tested (Johannsen & Psaltis 2010)? Do we live in a string axiverse filled with light axions (Arvanitaki et al. 2010)?

There have been two prior estimates of J1550's spin from X-ray measurements. The first of these, $a_* \approx 0$–0.1, was obtained using the CF method for a sample of 10 *Rossi X-ray Timing Explorer* (*RXTE*) spectra by Davis, Done & Blaes (2006). Their result was based on an old dynamical model and derived using approximate values of M, i and D (e.g. D was uncertain by ≈45 per cent; Orosz et al. 2002). We improve upon the work of Davis et al. by using our new dynamical model (e.g. with its four-fold better determination of D) and an approximately six times larger sample of *RXTE* spectra, and by our detailed treatment of observational and model-dependent uncertainties. A second measurement of J1550's spin was performed by Miller et al. (2009b) in a forward-looking work that combined Fe Kα and disc-continuum techniques in a preliminary study of eight sources. Their measurements were driven by constraints from the shape of the Fe Kα component, and the spin was measured to be $a_* \approx 0.76$. Our work differs in that we have applied both methods independently, and by doing so we have been able to treat a much larger data set and also select the most reliable data suited to each method.

In this paper, we present the spin of J1550 on two fronts. After introducing the data sets (Section 2), we begin by first applying the CF technique (Sections 3 and 4). This work is complemented with a thorough exploration of the statistical and systematic uncertainties inherent to the CF method (Section 5). Next, we measure the spin of J1550 using the Fe Kα technique (Section 6), and we finish with a discussion of the results (Section 7) and our conclusions (Section 8).

[1] BH spin is commonly expressed in terms of the dimensionless quantity $a_* \equiv a/M = cJ/GM^2$, where M and J are, respectively, the BH mass and angular momentum (Shapiro & Teukolsky 1983). Its limiting value is $a_* = +1$ (-1) for a maximal Kerr hole rotating in a prograde (retrograde) sense relative to the accretion disc; $a_* = 0$ corresponds to a non-spinning Schwarzschild hole.

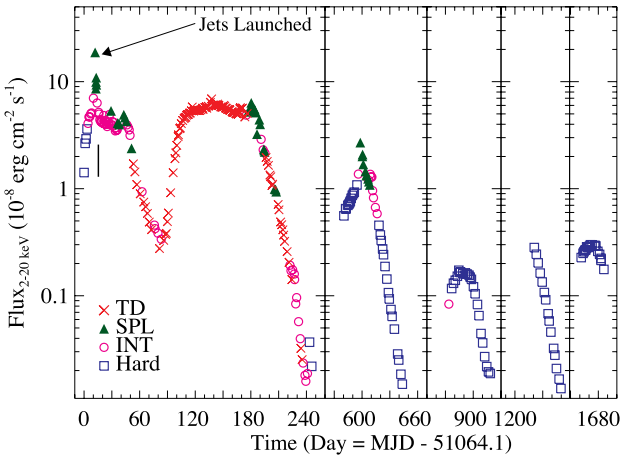

Figure 1. A spectral-state-encoded 2–20 keV light curve showing all five outburst cycles of J1550. Most disc-dominated data were obtained during the primary outburst in 1998–99. The time of the *ASCA* observation, which is analysed in Section 6, is marked at day 15 by the solid black line. The powerful 7-Crab flare near day 12 was responsible for the ejection of superluminal radio jets.

2 OBSERVATIONS

The primary data set used in this study is a compendium of 347 *RXTE* observations. The data include those obtained during the bright discovery outburst in 1998–99 on through four additional minor outbursts, the last ending in mid-2003. A light curve of the flux, showing the spectral evolution of the source, is presented in Fig. 1, where the spectral-state assignments have been determined using precisely the model, procedures and criteria described in Remillard & McClintock (2006). Thermal-dominant data, which are of primary importance for CF spin measurements, were obtained exclusively during the first outburst cycle.

RXTE spectral data are collected using PCU-2, the best calibrated and most frequently operating of the five Proportional Counter Array (PCA) detectors. Spectra are individually obtained by grouping sequential observations into approximately half-day bins, each with a typical exposure time ∼3 ks. We follow the procedures described in McClintock et al. (2006): the data are background subtracted, a customary 1 per cent systematic error in the data count rates is included, and a dead time correction ranging from approximately 1 to 20 per cent is applied. Spectra are fitted over the energy range 2.55–45 keV using XSPEC version 12.4–12.6 (Arnaud 1996). Calibration over this range is achieved using the latest version of PCARMF (v11.7).[2]

A linear collimator correction (assuming an ideal 1° triangular response; Jahoda et al. 2006) has been applied to the data set to account for a series of offsets in the PCA pointing. Specifically, we normalized the flux upwards by 4.4 per cent (2.67 arcmin offset) during the 1998–99 outburst and by 7.1 per cent (4.28 arcmin offset) during the 2000 outburst. After 2001 April, the correction is just ∼0.1 per cent. In addition to these global corrections, a handful of observations taken between 1998 September 7–9 and on 1999 January 6 were off-target for unknown reasons by $\approx 0\overset{\circ}{.}2$ and required us to make large corrections (for details, see Steiner et al. 2009a). We estimate that the uncertainty in these flux corrections is no more than 1–2 per cent, which has a negligible impact on our spectral fitting results.

In addition to the *RXTE* data set, we also include a 25-ks *ASCA* Gas Imaging Spectrometer (GIS) observation taken on UT 1998 September 23 when the source was in an INT state (see the observation time in Fig. 1 marked by the black vertical line). Following Miller et al. (2009b) and Miller et al. (2005), we use these *ASCA* data, with twice the resolution of the *RXTE* PCA data, to examine the iron line. However, we do not report a CF analysis on these data because the Compton component in the X-ray spectrum is too strong. We use standard data products for the GIS-2 and GIS-3 spectra with version 4.0 response matrices. The two spectra are fitted jointly over the 1–10 keV energy range, and in Section 6, we present our analysis of these data using the Fe Kα method.

3 CONTINUUM-FITTING ANALYSIS

We first enumerate our CF data-selection requirements and define two tiers of data quality. Next, we introduce the first and principal of three Comptonized accretion-disc models which are applied to the *RXTE* data set. Then, in the following section, we introduce two alternative models that differ principally in their treatment of the Compton reflection component. We find very close agreement in the spin estimate using all three models.

3.1 *RXTE* data selection

We identify two tiers of quality in our data based largely on the strength of the disc component relative to the Compton component. First-class 'gold' spectra are selected from just the strongly disc-dominated TD-state observations (the most reliable for measuring spin via the CF method; e.g. Shafee et al. 2006). In these spectra, the Compton component is only a few per cent or less of the total photon flux. We additionally consider a set of second-tier 'silver' spectra in which Comptonization is significantly stronger. These are selected from SPL-state and INT-state observations. The *gold* and *silver* spectra for J1550 are discussed and identified in an earlier study by our group, which we now briefly describe.

In Steiner et al. (2009a), we examined both J1550 and the BH candidate H1743−322, while comparing several models for the Compton power-law component (POWERLAW, COMPTT and SIMPL), and using for J1550 the same data set considered in this work. For *gold* spectra, we showed that our spin results are weakly dependent on the choice of the Comptonization model, whereas for *silver* spectra, only SIMPL both adequately models the Compton power law and provides consistent measurements of $r_{\rm in}$. The SIMPL model achieves this performance because it ensures photon conservation and self-consistently generates the power-law component of the spectrum using the disc component as input. Following Steiner et al., we here consider only those SPL and INT spectra with strong thermal components that have power-law normalizations $f_{\rm SC} < 25$ per cent, roughly an order of magnitude greater than typical for the TD state.

For a spectrum to be classified as either *gold* or *silver*, it must meet the following requirements: (1) goodness of fit, $\chi^2/\nu < 2$; (2) $r_{\rm in}$, the parameter of interest, is determined to a precision of $r_{\rm in}/\sigma_{r_{\rm in}} > 5$; and (3) the disc luminosity lies in the range 5–30 per cent $L_{\rm Edd}$. The lower luminosity threshold eliminates spectra that are associated with either advective flows (Esin, McClintock & Narayan 1997) or coronal feedback effects (e.g., Beloborodov 1999). The upper luminosity threshold ensures the disc is geometrically thin (McClintock et al. 2006; Penna et al. 2010), as required by the model. The adoption of this upper limit is supported by studies of

[2] http://www.universe.nasa.gov/xrays/programs/rxte/pca/doc/rmf/pcarmf-11.7/

slim-disc accretion (high-luminosity disc solutions) by Sądowski et al. (2011). They show that slim-disc and scaleheight effects cause significant deviations from the Novikov-Thorne solutions above $L_{\rm D}/L_{\rm Edd} \gtrsim 0.1$–$0.5$.

3.2 Results I: CF using SMEDGE

In selecting our CF data and then determining spin, we employ a variant of the principal model from our earlier study of J1550 and H1743–322 (hereinafter Model S; Steiner et al. 2009a): CRABCOR × TBABS × SMEDGE(SIMPL⊗KERRBB2). The custom multiplicative component CRABCOR corrects the response of the PCA detector to the Toor & Seward spectrum of the Crab (see Toor & Seward 1974; Steiner et al. 2010). TBABS (Wilms, Allen & McCray 2000) is a model of low-energy photoelectric absorption for which we fix the column density of J1550 to a high-precision measurement made using *Chandra* grating data: $N_{\rm H} = 8.0^{+0.4}_{-0.3} \times 10^{21}$ cm^{-2} (90 per cent confidence; Miller et al. 2003).

The key component of this model is KERRBB2 (McClintock et al. 2006), a fully relativistic thin accretion-disc model, which includes the self-irradiation of the disc ('returning radiation') and limb darkening (Li et al. 2005). The effects of spectral hardening are incorporated via a pair of look-up tables for the hardening factor f (Davis et al. 2005; Davis & Hubeny 2006) corresponding to two representative values of the viscosity parameter: $\alpha = 0.01$ and 0.1. Here and throughout, motivated by the results of both observational data and global general-relativistic magnetohydrodynamic (GRMHD) simulations (Penna et al. 2010; King, Pringle & Livio 2007, and references therein), we adopt $\alpha = 0.1$ as our fiducial value. Following our previous work, we use a zero-torque inner boundary condition and assume the alignment of the BH spin-axis with the binary orbital plane; we turn on both limb-darkening and returning radiation flags and fix the KERRBB2 normalization to unity. We fix the input parameters M, i and D to their nominal values (Section 1). The model KERRBB2 has just two fit parameters, namely the BH spin a_* and the mass-accretion rate $\dot{M}$, which can be reparametrized uniquely and equivalently as $r_{\rm in}$ and $L_{\rm D}/L_{\rm Edd}$ (the Eddington-scaled bolometric disc luminosity; McClintock et al. 2006).

We model the high-energy power law by convolving the thermal component with SIMPL(Steiner et al. 2009b), a model that mimics the physics of the Compton scattering of thermal disc photons by a hot corona. The model SIMPL converts a fraction $f_{\rm SC}$ of the seed photons into a power law with the photon index Γ. We use the standard, upscattering-only version. For the reflected component, we assume here that the disc elastically backscatters all incident Compton photons (generated by SIMPL), apart from a broad iron absorption edge feature that is modelled phenomenologically using SMEDGE (Ebisawa et al. 1994). The parameters of SMEDGE are the edge energy $E_{\rm Edge}$ (fitted from 7 to 9 keV), its optical depth $\tau_{\rm max}$ (unconstrained in the fit) and the width of the feature $W_{\rm Edge}$ (fixed at 7 keV). In the section that follows, we consider two models of reflection that are more physically motivated.

Applying our selection criteria to the full spectral model yields 35 *gold* spectra, where most of the winnowing is a result of our thin-disc limit on the intrinsic luminosity (i.e. prior to scattering) of the accretion-disc component: $L_{\rm D}/L_{\rm Edd} < 0.3$. We additionally select 25 *silver* spectra, 13 of which correspond to SPL-state observations and 12 to INT-state observations. Our spectral-fitting results are summarized in Table 1 (*gold* spectra correspond to entries 1–35 and *silver* spectra to entries 36–60).

For all these selected data, in Fig. 2, we plot a_* versus the luminosity of the disc component $L_{\rm D}/L_{\rm Edd}$. In a departure from our earlier work, in addition to a_*, we also plot the inner disc radius $R_{\rm in}$. The two quantities are equivalent in the sense that they are simply related to each other via a monotonic analytical formula (Section 1). We have chosen to also show $R_{\rm in}$ because it is the quantity that is more directly determined via CF.

Fig. 2 shows that the *gold* and *silver* data sets give results that are in good agreement. The net weighted result for the combined data set is $a_* = 0.23 \pm 0.07$ ($r_{\rm in} = 5.22 \pm 0.24$). The *gold* data give a slightly lower value for the spin, $a_* = 0.20$, than do the *silver* data, $a_* = 0.27$; the corresponding shifts from the mean value of $r_{\rm in}$ are, respectively, $+2$ and -3 per cent.

Although the data are clustered within a few per cent of a central value of $r_{\rm in}$, a small $\sim$5 per cent increase in $r_{\rm in}$ is observed with increasing $L_{\rm D}$, which is most pronounced for $L_{\rm D}/L_{\rm Edd} > 0.2$. This pattern has been previously observed for other sources (e.g. GRS 1915+105, McClintock et al. 2006; LMC X−3, Steiner et al. 2010). We tentatively attribute this effect to a thickening of the disc with luminosity and the limitation of our razor-thin disc model.

4 CONTINUUM FITTING: TOWARDS A SELF-CONSISTENT DISC + REFLECTION MODEL

In the previous section, we used the empirical model SMEDGE to crudely account for a prominent spectral feature in the reflection component, namely the broad K edge of iron. We now consider a more physically motivated treatment of the full reflection spectrum, which is generated by that portion of the power-law flux that strikes the accretion disc (Ross & Fabian 1993). To this end, we first consider a generalized version of SIMPL that is more appropriate to the problem at hand. We then examine two reflection models, IREFLECT and REFLIONX, concluding that the former model is better for CF fitting, while the latter model is better for fitting the profile of the Fe Kα line (which is considered in Section 6). As we describe below, there is presently no unified reflection model that is well suited to both approaches of measuring spin.

4.1 A variant of the power-law model SIMPL

As in Section 3, the core of our Comptonized-disc model consists of KERRBB2 and SIMPL. However, we now introduce a modified version of SIMPL that is appropriate when including a separate and additive reflection component. This model, SIMPL-R, is a generalization of SIMPL that covers the two limiting cases described by equations (1) and (2) in Steiner et al. (2009b), and applies to intermediate cases as well:

$$n_{\rm out}(E){\rm d}E = (1 - f_{\rm SC})n_{\rm in}(E)\,{\rm d}E + \left(\frac{f_{\rm SC}}{x}\right)\left[\int_{E_{\rm min}}^{E_{\rm max}} n_{\rm in}(E_0)G(E;E_0)\,{\rm d}E_0\right]{\rm d}E. \quad (1)$$

Here, $n_{\rm in}(E)$ and $n_{\rm out}(E)$ are the seed input and model output photon number densities at energy (E). The normalization constant $f_{\rm SC}$ is again the fraction of photons directed into a power law with the photon index Γ and $G(E;E_0)$ is the distribution function of the output power law (see Ebisawa 1999; Steiner et al. 2009b). The one new parameter is x, which determines the fraction of the power-law photons that strike the disc. *These are the photons which will be considered in modelling the reflection component.*

The standard version of SIMPL, which was used in the preceding section, assumes either that none of the Compton-scattered photons strikes the disc or adopting an equivalent interpretation that

Table 1. Model S CF results.

N	MJD	$\frac{L_D}{L_{Edd}}$	SMEDGE		SIMPL		KERRBB2		χ^2_ν/d.o.f.	State
			E_{Edge} (keV)	τ_{max}	Γ	f_{SC}	a_*	$\dot{M}$ (10^{18} g s^{-1})		
1	51117.4	0.172±0.003	8.3 ± 0.1	1.1 ± 0.2	2.06 ± 0.03	0.029 ± 0.002	0.24 ± 0.02	3.30 ± 0.11	0.7/74	TD
2	51119.0	0.155±0.002	8.1 ± 0.1	1.3 ± 0.2	2.11 ± 0.03	0.030 ± 0.002	0.22 ± 0.02	3.01 ± 0.09	0.8/74	TD
3	51121.0	0.136±0.002	8.3 ± 0.1	1.5 ± 0.3	2.15 ± 0.06	0.011 ± 0.001	0.23 ± 0.02	2.62 ± 0.07	0.7/74	TD
4	51124.7	0.115±0.002	8.1 ± 0.1	1.7 ± 0.2	2.15 ± 0.04	0.023 ± 0.001	0.22 ± 0.02	2.25 ± 0.08	0.6/74	TD
5	51128.6	0.101±0.002	7.9 ± 0.1	1.7 ± 0.1	2.17 ± 0.03	0.036 ± 0.001	0.16 ± 0.04	2.04 ± 0.10	1.0/74	TD
6	51130.5	0.094±0.002	8.0 ± 0.1	1.7 ± 0.1	2.17 ± 0.02	0.038 ± 0.001	0.15 ± 0.03	1.92 ± 0.09	1.3/74	TD
7	51132.5	0.086±0.002	7.8 ± 0.1	1.7 ± 0.1	2.16 ± 0.02	0.035 ± 0.001	0.16 ± 0.03	1.75 ± 0.09	0.8/74	TD
8	51134.5	0.080±0.002	7.7 ± 0.1	1.9 ± 0.1	2.28 ± 0.03	0.027 ± 0.001	0.16 ± 0.03	1.63 ± 0.08	0.8/74	TD
9	51136.9	0.072±0.001	7.8 ± 0.1	2.0 ± 0.1	2.16 ± 0.03	0.025 ± 0.001	0.19 ± 0.03	1.42 ± 0.07	0.9/74	TD
10	51145.5	0.053±0.001	7.9 ± 0.1	1.8 ± 0.1	2.05 ± 0.02	0.025 ± 0.001	0.26 ± 0.04	1.01 ± 0.06	0.7/74	TD
11	51150.1	0.059±0.001	7.6 ± 0.1	1.8 ± 0.1	2.08 ± 0.03	0.030 ± 0.001	0.22 ± 0.03	1.15 ± 0.06	0.9/74	TD
12	51152.1	0.069±0.001	7.9 ± 0.1	2.6 ± 0.3	2.13 ± 0.07	0.015 ± 0.001	0.22 ± 0.02	1.33 ± 0.05	0.8/74	TD
13	51152.9	0.066±0.001	8.2 ± 0.1	3.3 ± 0.3	2.20 ± 0.08	0.010 ± 0.001	0.31 ± 0.02	1.21 ± 0.04	0.8/74	TD
14	51154.0	0.082±0.001	7.8 ± 0.2	2.8 ± 0.4	2.39 ± 0.13	0.012 ± 0.002	0.22 ± 0.03	1.60 ± 0.06	0.7/74	TD
15	51155.1	0.092±0.001	8.4 ± 0.2	2.1 ± 0.4	2.43 ± 0.13	0.008 ± 0.001	0.24 ± 0.02	1.75 ± 0.06	0.7/74	TD
16	51157.6	0.122±0.002	8.6 ± 0.4	1.3 ± 0.6	2.75 ± 0.25	0.007 ± 0.002	0.25 ± 0.02	2.33 ± 0.07	0.8/74	TD
17	51160.3	0.165±0.002	7 ± 3	0.1 ± 0.2	1.94 ± 0.27	0.002 ± 0.001	0.25 ± 0.01	3.15 ± 0.07	0.7/74	TD
18	51162.2	0.213±0.002	7.6 ± 0.1	1.4 ± 0.3	3.1 ± 0.7	0.004 ± 0.004	0.17 ± 0.02	4.29 ± 0.10	1.1/74	TD
19	51163.2	0.233±0.003	7.2 ± 0.2	1.6 ± 0.3	3.2 ± 1.3	0.004 ± 0.008	0.15 ± 0.02	4.74 ± 0.13	0.7/74	TD
20	51164.2	0.267±0.002	7.0 ± 0.3	1.3 ± 0.2	2.3 ± 1.1	0.001 ± 0.003	0.12 ± 0.02	5.55 ± 0.11	1.0/74	TD
21	51260.6	0.193±0.003	8.1 ± 0.1	1.1 ± 0.2	2.06 ± 0.04	0.030 ± 0.002	0.21 ± 0.02	3.77 ± 0.12	0.4/66	TD
22	51261.8	0.180±0.003	8.4 ± 0.2	1.0 ± 0.2	2.03 ± 0.03	0.029 ± 0.002	0.23 ± 0.02	3.48 ± 0.11	0.7/66	TD
23	51263.1	0.173±0.003	8.1 ± 0.1	1.4 ± 0.2	2.13 ± 0.03	0.036 ± 0.002	0.16 ± 0.04	3.51 ± 0.16	0.6/66	TD
24	51264.8	0.148±0.002	8.2 ± 0.1	1.6 ± 0.1	2.07 ± 0.03	0.031 ± 0.001	0.21 ± 0.03	2.89 ± 0.10	0.7/66	TD
25	51265.6	0.141±0.003	8.3 ± 0.1	1.4 ± 0.1	2.09 ± 0.03	0.035 ± 0.002	0.22 ± 0.03	2.75 ± 0.10	0.8/66	TD
26	51266.9	0.128±0.002	8.2 ± 0.1	1.6 ± 0.2	2.12 ± 0.03	0.024 ± 0.001	0.23 ± 0.02	2.46 ± 0.09	0.5/66	TD
27	51267.6	0.128±0.003	8.1 ± 0.1	1.8 ± 0.1	2.13 ± 0.02	0.040 ± 0.001	0.18 ± 0.04	2.54 ± 0.12	0.9/66	TD
28	51273.6	0.097±0.002	8.1 ± 0.1	1.8 ± 0.1	2.17 ± 0.02	0.040 ± 0.001	0.15 ± 0.04	1.96 ± 0.10	0.7/66	TD
29	51274.5	0.092±0.002	7.9 ± 0.1	1.9 ± 0.1	2.12 ± 0.03	0.033 ± 0.001	0.14 ± 0.04	1.89 ± 0.10	0.7/66	TD
30	51276.3	0.081±0.002	8.0 ± 0.1	2.6 ± 0.2	2.04 ± 0.05	0.019 ± 0.001	0.18 ± 0.05	1.61 ± 0.10	0.6/66	TD
31	51277.4	0.075±0.002	8.0 ± 0.1	2.2 ± 0.1	2.07 ± 0.03	0.026 ± 0.001	0.20 ± 0.03	1.48 ± 0.08	1.0/66	TD
32	51278.7	0.071±0.002	7.8 ± 0.1	2.0 ± 0.2	2.11 ± 0.04	0.027 ± 0.001	0.17 ± 0.05	1.44 ± 0.10	0.7/66	TD
33	51279.6	0.066±0.002	7.9 ± 0.1	2.2 ± 0.1	2.06 ± 0.03	0.023 ± 0.001	0.21 ± 0.03	1.30 ± 0.06	0.8/66	TD
34	51280.6	0.060±0.002	8.1 ± 0.1	2.2 ± 0.2	2.06 ± 0.04	0.021 ± 0.001	0.23 ± 0.03	1.17 ± 0.06	0.7/66	TD
35	51283.2	0.057±0.002	7.4 ± 0.2	1.6 ± 0.2	2.21 ± 0.05	0.027 ± 0.002	0.13 ± 0.06	1.17 ± 0.10	0.6/66	TD
36	51110.3	0.252±0.001	8.3 ± 0.1	1.1 ± 0.1	2.55 ± 0.02	0.223 ± 0.007	0.15 ± 0.05	5.13 ± 0.25	0.8/74	INT
37	51111.6	0.234±0.003	8.1 ± 0.1	1.1 ± 0.1	2.50 ± 0.02	0.240 ± 0.009	0.14 ± 0.06	4.79 ± 0.27	0.8/74	INT
38	51112.8	0.224±0.001	8.1 ± 0.1	1.2 ± 0.1	2.51 ± 0.02	0.249 ± 0.008	0.10 ± 0.06	4.70 ± 0.29	0.8/74	INT
39	51113.7	0.206±0.003	8.3 ± 0.1	1.2 ± 0.1	2.49 ± 0.02	0.208 ± 0.008	0.21 ± 0.04	4.03 ± 0.20	1.0/74	INT
40	51115.3	0.172±0.002	8.4 ± 0.1	1.3 ± 0.1	2.42 ± 0.02	0.153 ± 0.005	0.30 ± 0.03	3.14 ± 0.14	0.8/74	SPL
41	51126.6	0.110±0.002	8.2 ± 0.1	1.7 ± 0.1	2.29 ± 0.02	0.059 ± 0.001	0.17 ± 0.04	2.21 ± 0.11	1.0/74	INT
42	51140.0	0.056±0.001	8.0 ± 0.1	1.8 ± 0.1	2.17 ± 0.02	0.086 ± 0.002	0.32 ± 0.04	1.01 ± 0.07	1.0/74	INT
43	51140.7	0.055±0.001	8.1 ± 0.1	1.8 ± 0.1	2.19 ± 0.02	0.078 ± 0.002	0.31 ± 0.04	1.00 ± 0.07	1.1/74	INT
44	51143.8	0.052±0.001	8.0 ± 0.1	1.7 ± 0.1	2.21 ± 0.02	0.081 ± 0.003	0.28 ± 0.07	0.98 ± 0.10	0.8/74	INT
45	51269.7	0.117±0.002	8.2 ± 0.1	1.8 ± 0.1	2.25 ± 0.02	0.052 ± 0.001	0.17 ± 0.04	2.34 ± 0.13	1.0/66	SPL
46	51270.8	0.092±0.002	8.3 ± 0.1	1.6 ± 0.1	2.28 ± 0.01	0.110 ± 0.002	0.31 ± 0.03	1.68 ± 0.09	1.0/66	SPL
47	51271.4	0.086±0.002	8.3 ± 0.1	1.5 ± 0.1	2.30 ± 0.02	0.120 ± 0.003	0.32 ± 0.04	1.57 ± 0.09	0.9/66	SPL
48	51664.4	0.148±0.004	8.2 ± 0.1	1.5 ± 0.1	2.45 ± 0.02	0.165 ± 0.005	0.31 ± 0.04	2.70 ± 0.15	0.8/66	SPL
49	51664.7	0.145±0.004	8.4 ± 0.1	1.4 ± 0.1	2.42 ± 0.02	0.173 ± 0.005	0.35 ± 0.04	2.56 ± 0.15	0.9/66	SPL
50	51665.4	0.135±0.003	8.1 ± 0.1	1.5 ± 0.1	2.42 ± 0.02	0.145 ± 0.004	0.29 ± 0.05	2.50 ± 0.16	0.8/66	SPL
51	51667.7	0.119±0.003	8.2 ± 0.1	1.5 ± 0.1	2.36 ± 0.02	0.126 ± 0.003	0.33 ± 0.03	2.15 ± 0.11	0.7/66	SPL
52	51668.8	0.115±0.003	8.2 ± 0.1	1.5 ± 0.1	2.34 ± 0.02	0.117 ± 0.003	0.32 ± 0.03	2.08 ± 0.10	1.0/66	SPL
53	51669.2	0.123±0.003	8.1 ± 0.1	1.6 ± 0.1	2.38 ± 0.02	0.109 ± 0.003	0.23 ± 0.04	2.38 ± 0.13	1.1/66	SPL
54	51670.6	0.102±0.003	8.1 ± 0.1	1.6 ± 0.1	2.35 ± 0.02	0.143 ± 0.003	0.32 ± 0.04	1.85 ± 0.11	0.8/66	SPL
55	51670.8	0.107±0.003	8.3 ± 0.1	1.6 ± 0.1	2.33 ± 0.02	0.113 ± 0.003	0.31 ± 0.03	1.95 ± 0.10	0.8/66	INT
56	51671.4	0.111±0.003	8.0 ± 0.1	1.7 ± 0.1	2.35 ± 0.02	0.108 ± 0.003	0.23 ± 0.04	2.14 ± 0.13	1.1/66	SPL
57	51672.4	0.096±0.003	8.2 ± 0.1	1.7 ± 0.1	2.31 ± 0.02	0.121 ± 0.003	0.32 ± 0.04	1.75 ± 0.10	0.8/66	SPL
58	51673.0	0.097±0.004	8.2 ± 0.1	1.5 ± 0.1	2.39 ± 0.01	0.205 ± 0.005	0.35 ± 0.06	1.71 ± 0.14	0.7/66	INT
59	51673.4	0.099±0.004	8.1 ± 0.1	1.6 ± 0.1	2.42 ± 0.01	0.196 ± 0.004	0.28 ± 0.07	1.84 ± 0.17	0.8/66	INT
60	51674.7	0.085±0.004	8.1 ± 0.1	1.4 ± 0.1	2.31 ± 0.02	0.224 ± 0.006	0.37 ± 0.08	1.48 ± 0.16	0.6/66	INT

Notes. Reported error estimates are symmetric 1σ statistical uncertainties. M, i and D are frozen at their fiducial values.

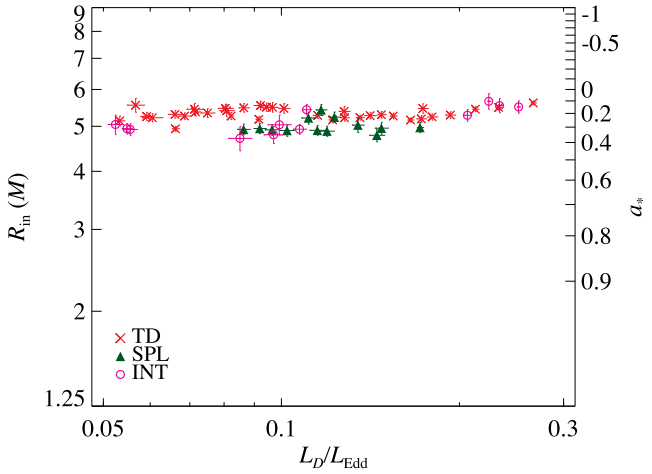

Figure 2. The spin, expressed in terms of both $R_{\rm in}$ and a_*, versus luminosity. The TD spectra comprise the *gold* data set, and the INT and SPL spectra comprise the *silver* data set. The mean value of $R_{\rm in}$ is in agreement for the two data sets to within ≈5 per cent even though the Compton component is much stronger for the *silver* data. The error bars represent statistical uncertainties from X-ray spectral fitting only; they do not include the additional sources of error discussed in Section 5.

reflection acts like a perfect mirror with no absorption. This corresponds to the limiting case $x = 1$, which is described by equation (1) in Steiner et al. (2009b). In the opposite limit, $x = 2$, half of the scattered photons are redirected downwards, illuminating the disc, while failing to reach an observer at infinity, As they encounter the disc atmosphere, the returning photons are absorbed and reprocessed, thereby generating the reflection component. This limit corresponds to equation (2) in Steiner et al. (2009b).

The variant SIMPL-R (equation 1) generalizes this dichotomy, making it possible to treat separately the reprocessed emission coming from the illuminated disc via the tunable parameter x. This allows one to model a corona quite generally. The quantity $x - 1$ describes the solid angle subtended by the disc from the perspective of the corona in units of 2π, which we refer to as a covering factor. In this paper, we assume that the geometry of the corona is a disc-hugging slab with a covering factor of unity ($x = 2$); thus, half the photons escape the system and half strike the disc. As shorthand, we will refer to the portion of the Compton component produced by SIMPL-R which irradiates the disc as SIMPLC [i.e. the second term on the right-hand side of equation (1) multiplied by the covering factor].

4.2 Results II: CF using IREFLECT and REFLIONX

We first consider the model IREFLECT (Magdziarz & Zdziarski 1995), which computes the reflected spectrum (including scattering and edge absorption, but excluding line fluorescence) generated in an ionized disc atmosphere that is illuminated by an arbitrary external spectrum. We convolve the disc-illuminating component SIMPLC with IREFLECT and isolate the reflected component by setting the parameter rel_refl to -1. (Our model implicitly assumes that the observed and illuminating power-law spectra are identical.) The ionization parameter $\xi \equiv L/nR^2$ is initially set to 10^4 and allowed to vary freely from 10^1 to 10^5, while the characteristic disc temperature is fixed to $T_{\rm disc} = 5 \times 10^6$ K and the metallicity is assumed to be solar. Fe Kα emission is included separately in an approximate fashion as an intrinsically narrow Gaussian line centred at the rest-frame energy of 6.5 keV. This composite reflection component is then convolved with the relativistic smearing kernel KERRCONV (Brenneman & Reynolds 2006) with the radial emissivity index q fixed at the best-fitting *RXTE* value $q = 2.5$ (see Section 6). The complete model, which is comprised of an accretion-disc and a power-law component, is CRABCOR×TBABS[SIMPL-R⊗KERRBB2 + KERRCONV⊗(IREFLECT⊗SIMPLC + GAUSS)].

The primary limitation of this model (hereinafter referred to as Model I) is that although edges are included, the fluorescent line features (e.g. García & Kallman 2010), apart from Fe Kα, are missing. Also, the strength of the Fe Kα feature should be tied to the depth of the corresponding edge feature, but here that is not possible. Below and in Section 5, we will demonstrate that these shortcomings of Model I have little effect on the CF spin results because for our primary *gold* spectra the reflected component is faint compared to the dominant thermal component. However, these issues are of critical importance in estimating spin via the Fe Kα line (Section 6).

We now consider a second reflection model, REFLIONX (Ross & Fabian 2005), which we use as a replacement for (IREFLECT⊗SIMPLC+GAUSS) in Model I given above. We will refer to the new composite model as Model R. In REFLIONX, reflection is produced by a power-law spectrum illuminating a cold slab of constant density. The virtue of this model is that it properly couples line emission to absorption, and it also describes the full Fe K emission-line complex. A major drawback is that it is optimized for modelling AGNs, which have cold discs of lower density. Consequently, in estimating spin via the Fe Kα method (Section 6), we use a high-density variant of REFLIONX, REFBHB, which includes an intrinsic blackbody component (Ross & Fabian 2007). Because the blackbody component is hardwired into REFBHB, it cannot presently be used with CF models. We therefore use REFLIONX in concert with KERRBB2 for our CF analysis.

In addition to the temperature/density limitations of REFLIONX just mentioned, this model has additional shortcomings. Of primary importance, it requires that the illuminating spectrum has a simple power-law form. This power law is not truncated at low energies and its flux can rival or exceed the thermal flux, thereby leading to unphysical results (see e.g. Steiner et al. 2009b). In addition, the strength of the reflected component is not linked to the normalization of the illuminating spectrum, and so there is no way to ensure that the Compton and reflection components are appropriately matched. Nevertheless, we employ Model R using REFLIONX as a second-tier CF model that gives us an independent check on the results obtained using Model I.

In summary, using a variant of SIMPL and considering two reflection models, we have progressed towards a model featuring a self-consistent treatment of thermal disc emission, Compton scattering and disc reflection. For estimating spin via the CF method, we favour IREFLECT, while for the Fe Kα method we elect to use REFLIONX and REFBHB (Section 6).

We now apply Model I (Section 4.2) to our set of *RXTE* spectra, while following the procedures described in Section 3.2. In this case, we find that only a total of 45 spectra (24 *gold* and 21 *silver*) meet our selection criteria (Section 3.1), compared to the 60 selected using Model S. Our fitting results for these 45 spectra are given in Table 2.

For the *gold* spectra, we find excellent agreement between the results obtained using Model I, $a_* = 0.23 \pm 0.06$, and Model S, $a_* = 0.20 \pm 0.04$. This agreement is illustrated in Fig. 3, where we also show results for Model R. As is apparent, considering only the *gold* spectra, all three models are in excellent agreement – the mean

Table 2. Model I CF results.

N	MJD	$\frac{L_D}{L_{Edd}}$	SIMPL-R		KERRBB2		IREFLECT	GAUSS	χ^2_ν/d.o.f.	State
			Γ	f_{sc}	a_*	$\dot{M}$ (10^{18} g s^{-1})	ξ (erg cm s^{-1})	N (photon cm^{-2} s^{-1})		
1	51117.4	0.175±0.002	2.04 ± 0.04	0.018 ± 0.002	0.24 ± 0.02	3.37 ± 0.11	1500 ± 1600	2.8 ± 2.7	0.7/74	TD
2	51119.0	0.156±0.002	2.07 ± 0.04	0.017 ± 0.002	0.23 ± 0.02	3.01 ± 0.09	1200 ± 1300	2.7 ± 2.0	0.7/74	TD
3	51121.0	0.136±0.002	2.06 ± 0.06	0.006 ± 0.001	0.24 ± 0.02	2.61 ± 0.07	2000 ± 3000	1.4 ± 1.1	0.7/74	TD
4	51124.7	0.115±0.002	2.07 ± 0.06	0.012 ± 0.002	0.24 ± 0.02	2.20 ± 0.07	1200 ± 2200	2.5 ± 1.5	0.6/74	TD
5	51128.6	0.098±0.001	2.09 ± 0.05	0.020 ± 0.003	0.24 ± 0.02	1.89 ± 0.07	1100 ± 1800	2.9 ± 1.5	0.9/74	TD
6	51130.5	0.092±0.001	2.15 ± 0.03	0.023 ± 0.001	0.22 ± 0.02	1.79 ± 0.05	310 ± 100	2.9 ± 0.9	1.1/74	TD
7	51132.5	0.082±0.001	2.07 ± 0.03	0.018 ± 0.001	0.25 ± 0.03	1.55 ± 0.07	1900 ± 1900	2.9 ± 1.2	0.8/74	TD
8	51134.5	0.075±0.001	2.15 ± 0.04	0.013 ± 0.001	0.26 ± 0.03	1.43 ± 0.06	1900 ± 2200	1.9 ± 0.8	0.8/74	TD
9	51136.9	0.068±0.001	2.08 ± 0.21	0.013 ± 0.008	0.28 ± 0.03	1.26 ± 0.07	700 ± 5000	2.0 ± 1.0	0.9/74	TD
10	51157.6	0.122±0.001	2.6 ± 0.7	0.004 ± 0.007	0.25 ± 0.02	2.33 ± 0.08	600 ± 10 000	0.5 ± 0.8	0.8/74	TD
11	51160.3	0.167±0.001	1.97 ± 0.32	0.001 ± 0.001	0.24 ± 0.02	3.21 ± 0.08	50 000 ± 700 000	0.0 ± 1.5	0.7/74	TD
12	51163.2	0.253±0.004	2.7 ± 1.3	0.001 ± 0.003	0.00 ± 0.03	5.62 ± 0.17	10 ± 4000	3.4 ± 3.0	1.7/74	TD
13	51260.6	0.194±0.002	1.97 ± 0.04	0.015 ± 0.001	0.22 ± 0.02	3.77 ± 0.11	6000 ± 5000	4.5 ± 3.0	0.4/66	TD
14	51261.8	0.183±0.003	2.04 ± 0.04	0.018 ± 0.002	0.22 ± 0.02	3.56 ± 0.12	1500 ± 1600	2.4 ± 2.9	0.7/66	TD
15	51263.1	0.174±0.002	2.07 ± 0.04	0.020 ± 0.002	0.18 ± 0.03	3.48 ± 0.15	1900 ± 1800	4.7 ± 3.0	0.5/66	TD
16	51264.8	0.153±0.002	1.97 ± 0.03	0.014 ± 0.001	0.18 ± 0.03	3.06 ± 0.12	6000 ± 4000	7.2 ± 1.9	0.8/66	TD
17	51265.6	0.144±0.002	2.10 ± 0.08	0.022 ± 0.004	0.22 ± 0.02	2.79 ± 0.09	500 ± 1000	3.3 ± 1.5	0.7/66	TD
18	51266.9	0.128±0.002	2.08 ± 0.23	0.014 ± 0.008	0.25 ± 0.03	2.45 ± 0.12	700 ± 5000	2.6 ± 2.0	0.5/66	TD
19	51267.6	0.127±0.002	2.08 ± 0.17	0.022 ± 0.009	0.22 ± 0.03	2.47 ± 0.13	700 ± 4000	4.9 ± 2.6	0.8/66	TD
20	51273.6	0.099±0.003	1.95 ± 0.03	0.015 ± 0.001	0.18 ± 0.04	1.97 ± 0.10	10 000 ± 9000	8.1 ± 1.4	1.9/66	TD
21	51274.5	0.087±0.001	2.04 ± 0.10	0.018 ± 0.005	0.24 ± 0.03	1.68 ± 0.08	800 ± 3000	3.1 ± 1.6	0.8/66	TD
22	51276.3	0.078±0.002	1.99 ± 0.19	0.010 ± 0.004	0.25 ± 0.03	1.48 ± 0.07	500 ± 3000	2.6 ± 0.7	0.7/66	TD
23	51278.7	0.062±0.002	1.92 ± 0.06	0.011 ± 0.001	0.34 ± 0.03	1.11 ± 0.06	20 000 ± 50 000	3.6 ± 1.2	0.8/66	TD
24	51279.6	0.060±0.001	1.99 ± 0.31	0.013 ± 0.011	0.33 ± 0.02	1.07 ± 0.05	700 ± 7000	2.1 ± 1.1	0.8/66	TD
25	51110.3	0.262±0.001	2.45 ± 0.02	0.109 ± 0.005	0.23 ± 0.03	5.06 ± 0.20	4879 ± 2000	17 ± 9	0.8/74	INT
26	51111.6	0.247±0.001	2.39 ± 0.03	0.113 ± 0.006	0.22 ± 0.04	4.80 ± 0.23	7147 ± 4000	24 ± 11	0.7/74	INT
27	51113.7	0.221±0.002	2.43 ± 0.03	0.108 ± 0.007	0.23 ± 0.04	4.25 ± 0.24	2331 ± 1500	17 ± 9	0.9/74	INT
28	51115.3	0.181±0.003	2.39 ± 0.07	0.086 ± 0.011	0.32 ± 0.04	3.28 ± 0.26	875.9 ± 1700	9 ± 7	0.7/74	SPL
29	51126.6	0.110±0.001	2.14 ± 0.03	0.025 ± 0.001	0.23 ± 0.02	2.11 ± 0.08	10 000 ± 7000	8.8 ± 1.7	1.5/74	INT
30	51269.7	0.117±0.002	2.10 ± 0.03	0.022 ± 0.001	0.22 ± 0.02	2.26 ± 0.08	10 000 ± 8000	9.1 ± 1.9	1.4/66	SPL
31	51270.8	0.083±0.001	2.17 ± 0.03	0.053 ± 0.003	0.50 ± 0.02	1.28 ± 0.06	10 000 ± 7000	10.2 ± 2.5	1.6/66	SPL
32	51271.4	0.081±0.001	2.20 ± 0.03	0.059 ± 0.003	0.47 ± 0.04	1.29 ± 0.10	10 000 ± 7000	10 ± 3	1.2/66	SPL
33	51664.4	0.156±0.003	2.40 ± 0.04	0.090 ± 0.005	0.35 ± 0.03	2.78 ± 0.12	500 ± 600	10 ± 4	0.6/66	SPL
34	51664.7	0.152±0.002	2.40 ± 0.05	0.097 ± 0.007	0.41 ± 0.02	2.58 ± 0.13	500 ± 800	10 ± 4	0.9/66	SPL
35	51665.4	0.140±0.001	2.37 ± 0.13	0.079 ± 0.019	0.34 ± 0.05	2.49 ± 0.31	700 ± 3000	7 ± 6	0.6/66	SPL
36	51667.7	0.119±0.002	2.29 ± 0.03	0.067 ± 0.005	0.41 ± 0.03	2.00 ± 0.11	1500 ± 1300	8 ± 4	0.7/66	SPL
37	51668.8	0.118±0.001	2.32 ± 0.04	0.068 ± 0.005	0.37 ± 0.03	2.04 ± 0.11	500 ± 600	6.2 ± 2.1	0.8/66	SPL
38	51669.2	0.125±0.003	2.35 ± 0.02	0.063 ± 0.002	0.31 ± 0.02	2.27 ± 0.08	230 ± 90	7.6 ± 2.5	0.9/66	SPL
39	51670.6	0.103±0.002	2.30 ± 0.03	0.079 ± 0.004	0.42 ± 0.02	1.72 ± 0.07	500 ± 400	8.0 ± 2.3	0.7/66	SPL
40	51670.8	0.102±0.002	2.25 ± 0.03	0.060 ± 0.004	0.44 ± 0.03	1.68 ± 0.09	1700 ± 1300	7 ± 3	0.7/66	INT
41	51671.4	0.110±0.002	2.29 ± 0.13	0.058 ± 0.016	0.34 ± 0.04	1.96 ± 0.17	600 ± 2700	7.3 ± 2.5	0.9/66	SPL
42	51672.4	0.093±0.001	2.25 ± 0.10	0.067 ± 0.014	0.44 ± 0.04	1.53 ± 0.15	800 ± 2700	7 ± 4	0.7/66	SPL
43	51673.0	0.096±0.001	2.33 ± 0.07	0.109 ± 0.013	0.50 ± 0.05	1.49 ± 0.16	900 ± 1900	10 ± 6	0.6/66	INT
44	51673.4	0.098±0.002	2.36 ± 0.09	0.103 ± 0.017	0.44 ± 0.06	1.61 ± 0.23	900 ± 2500	10 ± 6	0.8/66	INT
45	51674.7	0.082±0.001	2.22 ± 0.03	0.113 ± 0.006	0.56 ± 0.05	1.20 ± 0.11	2600 ± 1800	11 ± 6	0.6/66	INT

values of r_{in} are consistent with one another to within ≈2 per cent. However, for the *silver* spectra, the mean values of r_{in} are depressed for all three models, by ≈10 per cent for the self-consistent reflection models (which track each other closely) and by only ≈5 per cent for Model S. Interestingly, the primitive Model S performs better than the self-consistent reflection models by harmonizing the results obtained from the two data sets and delivering the highest degree of internal consistency. Fig. 4 shows an overlay comparison of the best-fitting results using the three models for two representative spectra, one *gold* and the other *silver*. The total unfolded spectra and their components are plotted, as well as the data-to-model ratio. The key result of this section is that using our fiducial values of M, i and D (Section 1), all three models applied to the *gold* spectra give the same low estimate of spin: $0.15 < a_* < 0.35$.

5 CONTINUUM FITTING: ERROR ANALYSIS AND FINAL SPIN RESULT

In this section, we broadly consider three sources of observational error, both systematic and statistical, which bear on our final estimate of the spin. In order of increasing importance, these are (1) sensitivity to the details of the spectral models employed; (2) X-ray flux calibration uncertainties; and (3) the uncertainties in the input parameters M, i and D. We then perform a comprehensive

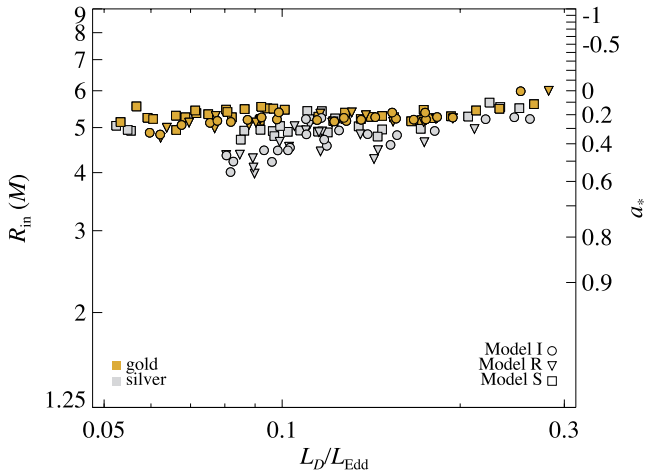

Figure 3. As in Fig. 2, we again plot $R_{\rm in}$ and a_* versus luminosity, but we now show results for all three of the models discussed in the text. The data for Model S, which are repeated from Fig. 2, show the highest degree of internal consistency.

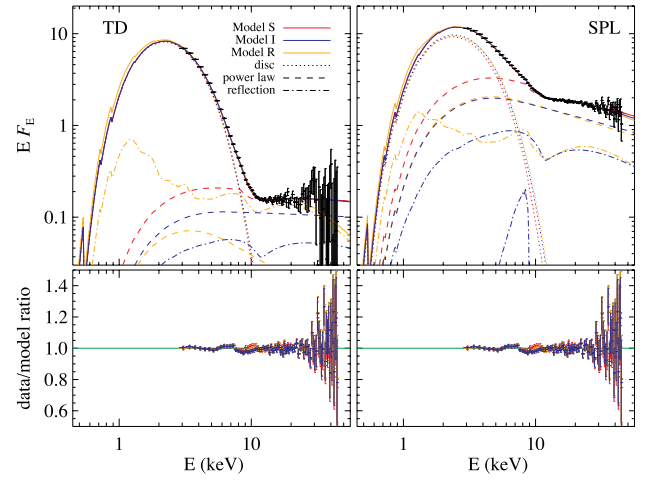

Figure 4. Model fits for a *gold* spectrum (left-hand panel) and a *silver* spectrum (right-hand panel), which correspond respectively to observations made on MJD 51121.0 and MJD 51115.3 (see Tables 1 and 2). The models are differentiated by line colour and the individual components by line texture. Note how much weaker the power-law component is for the *gold* spectrum and how closely all three models track the data.

analysis that incorporates these uncertainties and arrive at our final CF estimate of the spin of the BH. In the following, we present an overview; for details, see Appendix A.

(1) *Sensitivity to X-ray spectral models.* In order to make this assessment, we determine the change in $r_{\rm in}$ when varying a single model component or parameter setting. Table 3 gives the mean fractional change in $r_{\rm in}$ for the *gold* data sample that arises from changing either a model parameter (rows P1–P12) or a model component (M1–M5). The 'Change' column describes the alteration made to a parameter or model component relative to its nominal condition (where DISC, PL and REFL refer to the accretion-disc, power-law and reflection components). The third and fourth columns, respectively, list the fractional changes in $r_{\rm in}$ for Model I and Model S. As Table 3 demonstrates, the largest model uncertainty arises from the choice of the viscosity parameter: using $\alpha = 0.01$ instead of the default value ($\alpha = 0.1$) decreases $r_{\rm in}$ by $\approx$4 per cent for Model I and

Table 3. Systematic changes to the model.

TD	Change	$\Delta\bar{r}_{\rm in}$ (per cent)	
		Model I	Model S
P1	$\alpha = 0.01$	−3.68	−2.90
P2	$N_{\rm H} = 6 \times 10^{21}$ cm^{-2}	−2.90	−1.94
P3	$N_{\rm H} = 10 \times 10^{21}$ cm^{-2}	0.84	2.84
P4	$x = 1.5$	−1.13	–
P5	$x = 1.1$	−1.26	–
P6	q and x free	0.21	–
P7	$q = 3$	−2.88	–
P8	$T_{\rm disc} = 10^6$ K	−0.09	–
P9	$T_{\rm disc} = 10^7$ K	0.17	–
P10	$E_{\rm line} = 6.8$ keV	−1.86	–
P11	$W_{\rm Edge} = 3.5$ keV	–	−0.42
P12	$W_{\rm Edge} = 14$ keV	–	0.41
M1	DISC: BHSPEC	1.30	2.88
M2	PL: fall-off with $kT_{\rm e}$	−1.53	−0.66
M3	PL: downscattering set	−0.27	0.07
M4	REFL: SMEDGE	1.70	–
M5	REFL: REFLIONX	−1.00	−2.65

3 per cent for Model S. Each of the other 16 changes considered affects $r_{\rm in}$ by <3 per cent.

(2) *Flux calibration.* The problem of flux calibration is endemic to X-ray astronomy. The Crab spectrum, as determined by Toor & Seward (1974), is the widely adopted standard that we have consistently used in our work. Uncertainties in the normalization of this spectrum have recently been considered by Weisskopf et al. (2010). Using their fig. 1 as a guide, we adopt a generous ±10 per cent uncertainty in our overall flux calibration, which corresponds to a 5 per cent uncertainty in $r_{\rm in}$.

(3) *Uncertainties in M, i and D.* As in our earlier work (e.g. Liu et al. 2008; Gou et al. 2009, 2010), we sample the allowed parameter space assuming Gaussian errors (except here for D, we use an asymmetric Gaussian). The sampling is performed using 42 500 triplets of M, i and D, which are distributed in a uniform grid throughout the parameter space. At each point in the grid, the complete *RXTE* data set is analysed with Model S, and the selection criteria given in Section 3 are separately applied to the results. Folding all of the runs together, a composite distribution based on all of the selected spectra is obtained, where we have additionally weighted over the set of possible dynamical models (see table 1 in Orosz et al. 2011).

In conducting this analysis, we have included the robust no-eclipse constraint, $i < 82^\circ$. We have further required that during the TD-state plateau phase (days 105–182; Fig. 1) the disc luminosity does not exceed 85 per cent of $L_{\rm Edd}$ (the actual Eddington limit for disc geometry; see section 6.1 in McClintock et al. 2006). Lastly, we also require that the disc luminosity during the thermal plateau phase be greater than 10 per cent of $L_{\rm Edd}$, or else the full sample of TD data would extend downwards in luminosity to the implausibly low value of $\lesssim$0.1 per cent $L_{\rm Edd}$.

In the analysis described above, we have used the default value of the viscosity parameter, $\alpha = 0.1$. Because α is the major source of uncertainty considered in Table 3, we have repeated the analysis just described using $\alpha = 0.01$ and combined the two distributions, weighting them equally. We combine all other errors in Table 3, yielding an ensemble value of $\approx$4.2 per cent. Finally, we add in quadrature the 5 per cent error in the absolute flux calibration and

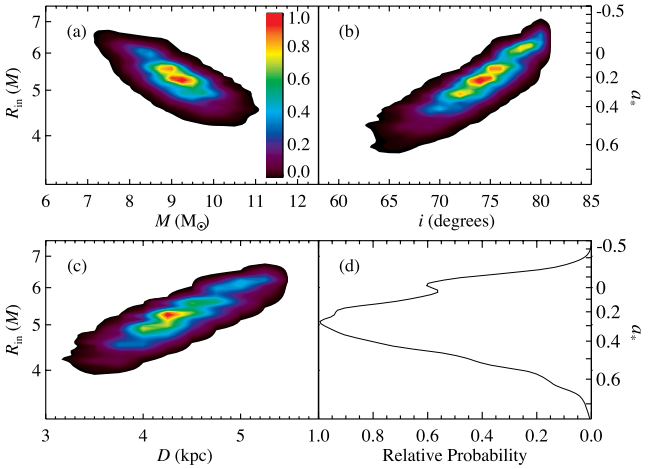

Figure 5. Probability contours for the relationship between r_{in}/spin, and M, i and D. Each of the first three panels (a–c) shows variation for a single parameter; the other two parameters have been fixed at their best values. The orientations of the probability ellipsoids show that spin is positively correlated with M and negatively correlated with both i and D. In panel (d), a combined probability distribution for the case $\alpha = 0.1$ is shown (arbitrarily scaled) with the variation in M, i and D folded together.

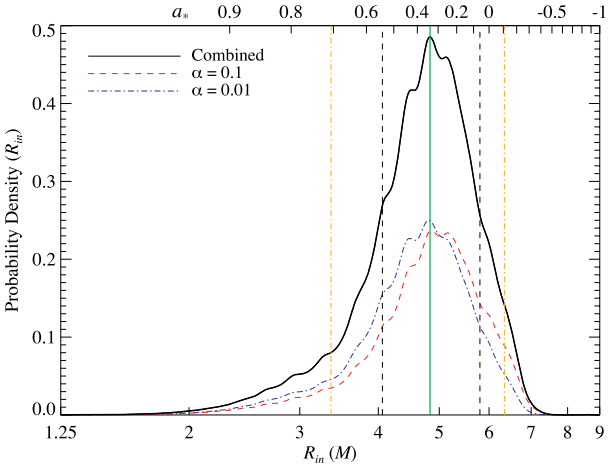

Figure 6. Composite probability density for R_{in} and a_* which takes into account both systematic and statistical errors, including uncertainties in distance, BH mass and inclination, the spectral model and the uncertainty in the absolute flux calibration. The net probability distribution is a combination of the individual distributions for two values of α. The contribution from each integrates to 50 per cent probability and is shown for $\alpha = 0.01$ (blue dot–dashed line) and $\alpha = 0.1$ (red-dashed line). The 90 per cent confidence limits for the combined distribution are shown as the yellow vertical lines, the 1σ limits as the vertical black lines and the most probable spin is marked with a green line. We conclude that the spin is moderate: $-0.11 < a_* < 0.71$ (90 per cent confidence).

arrive at our net error of 6.5 per cent. The effect of this uncertainty on our measurement of spin is incorporated by running a boxcar smoothing kernel (with a 13 per cent full width) over the distribution for r_{in}.

The dominant source of error in our final determination of the spin is the combined observational uncertainty in M, i and D, which in turn is largely a result of the uncertainties associated with modelling the optical/near-infrared light curves (Orosz et al. 2011). Fig. 5 shows the dependence of r_{in}/spin on these model parameters. Here, using the results of the grid analysis described above, we vary one of the three parameters, fixing the other two at the their best values. The strong correlations between spin and inclination, and between spin and distance, demonstrate the degree to which measurement errors in these quantities contribute to the uncertainty in spin. Together, errors in M, i and D account for $\Delta a_* \approx 0.25$ ($\Delta r_{in}/r_{in} \approx 0.2$) at 90 per cent confidence. The contribution due to the inclination is sizeable, ∼11 per cent for r_{in}, because its value is both large (74.°7) and uncertain (3.°8). The contribution due to the distance is also ∼11 per cent, while that due to the mass is only ∼7 per cent.

After folding together all sources of error, the resulting probability distribution is shown in Fig. 6, with R_{in} and a_* displayed, respectively, on the bottom and top axes. The green vertical line identifies the most probable spin, $a_* = 0.34$, and the yellow lines indicate the 90 per cent confidence interval, which extends from −0.11 to 0.71. From an inspection of this distribution function, we conclude that the BH is unlikely to be in a retrograde configuration (only ∼11.2 per cent probability). Of greater importance, we conclude that *the spin is not high*. For example, the probability that the CF spin exceeds 0.9 is less than 0.4 per cent, a surprising result for a BH that has produced superluminal jets.

6 SPIN FROM REFLECTION FEATURES

In the previous section, we concluded that the spin parameter has a low or intermediate value. This result is based on our CF analysis of many *RXTE* spectra, which were obtained primarily in the TD state. In what follows, we first analyse reflection features in INT-state spectra of J1550 obtained with the *ASCA X-ray Observatory*; we then supplement this analysis using a sample of *RXTE* spectra, also obtained in the INT state. We fit the *ASCA* GIS-2 and GIS-3 data simultaneously, using a floating normalization constant to allow for cross-calibration uncertainties. Our work differs from earlier analyses of the same data by others (e.g. see Gierliński & Done 2003; Miller et al. 2005, 2009b): our focus is on a detailed analysis of the reflection component, rather than on a precise model of the overall continuum. We begin by setting all the physical parameters of the binary to the best-estimate values presented in Orosz et al. (2011).

In addition to the soft disc and hard power-law components seen in the TD- and INT-state spectra of BH binaries, a broad emission line at ∼6.4 keV is also often present (see e.g. Miller 2007). This line feature is merely the most prominent reflection signature that arises as hard emission from the corona irradiates the cooler disc (Ross & Fabian 2005). In the vicinity of a BH, the Fe Kα line shape and other reflection features are distorted by various relativistic effects (Fabian et al. 1989; Laor 1991). The spin parameter can be constrained by modelling these features because their shape depends on how far the disc extends downwards into the gravitational potential well (see Section 1), the key assumption again being that this extent is set by the radius of the ISCO.

6.1 Phenomenological models – *ASCA*

In order to highlight the relativistic nature of the line profile in the *ASCA* spectra, we start by modelling the 1–4 and 7–10 keV continua with a combination of a disc blackbody (described by the XSPEC model DISKBB[3] of Mitsuda et al. 1984) and the Comptonization model SIMPL. The neutral hydrogen column was initially fixed at

[3] This model characterizes the thermal emission using only two parameters – the flux normalization and a colour temperature. Here, we use this very

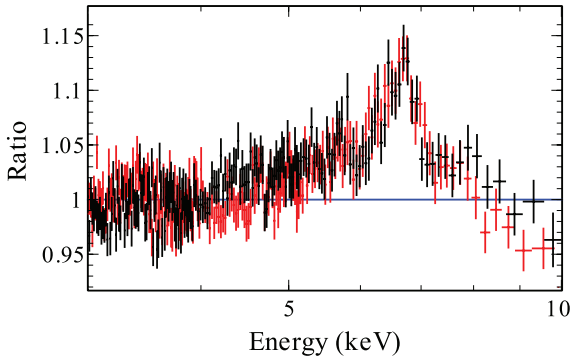

Figure 7. Data-to-model ratio for a phenomenological continuum model consisting of a thermal disc and a Compton component. *ASCA* GIS-2 and GIS-3 spectra are shown in black and red, respectively. The data were fitted jointly in the 1–4 and 7–10 keV energy range. The residuals in the 4–7 keV band show the relativistic nature (asymmetry and broadness) of the iron-emission-line profile. The data have been rebinned for plotting purposes. The data-to-model ratio for the full energy range is shown in Fig. 8.

$N_{\rm H} = 8 \times 10^{21}$ cm^{-2} as per Miller et al. (2003), which resulted in a poor fit to the continuum with $\chi^2/\nu = 2172.3/1002$. Allowing the column density to vary resulted in a significant improvement to the fit with $\chi^2/\nu = 1367.5/1001$ for $N_{\rm H} = (5.4 \pm 0.1) \times 10^{21}$ cm^{-2}. The total neutral hydrogen column density in the line of sight to J1550, which was determined using the *Chandra* transmission grating, is not expected to vary (Miller, Cackett & Reis 2009a). However, the differing values of $N_{\rm H}$ can be reasonably attributed to differences in the calibrations of the *Chandra* and *ASCA* detectors. Furthermore, allowing $N_{\rm H}$ to differ between the two GIS spectra further improves the fit: $\Delta\chi^2 = -47.5$ for one less degree of freedom with a difference in $N_{\rm H}$ of <5 per cent. Fig. 7 shows the line spectrum obtained by modelling the continuum as described above. The asymmetric and broad residual feature in the 4–7 keV band has the appearance one expects for fluorescent disc-line emission arising near a BH.

We provide a physical description of the Fe line by first modelling the residuals seen in Fig. 7 using the LAOR model (Laor 1991) and fitting for the inner radius $r_{\rm in}$ and the power-law index q of the emissivity profile, which is described by a power law of the form $\epsilon(r) \propto r^{-q}$. The outer disc radius is fixed at the maximum allowed value of $400 r_{\rm g}$ ($r_{\rm g} \equiv GM/c^2$), and the disc inclination is constrained to be approximately 1σ from the adopted value of Orosz et al. (2011) (i.e. between 71° and 78°). The line energy is constrained between 6.4 and 6.97 keV. The fit achieved by including the LAOR component, shown in Fig. 8, results in $\chi^2/\nu = 1848.0/1501$, an improvement of $\Delta\chi^2 = -416$ for 5 fewer degrees of freedom (compared to the best-fitting continuum model with no line feature). The best-fitting parameters for this model are detailed in Table 4 (Model 1).

It can be seen from the ratio plot shown in Fig. 8 that this simple, heuristic model, although mostly adequate, does not provide a detailed description of all the features present in the 6–8 keV range. Adding a narrow Gaussian line at ≈6.7 keV only marginally improves the fit[4] ($\Delta\chi^2 = -14.4$ for 2 fewer degrees of freedom), with evidence for additional residuals, which are possibly associated with Fe K-shell absorption edges in partially ionized material (Ross & Fabian 1993; Ross, Fabian & Brandt 1996). Such features

approximate model of the continuum (cf. Section 3) because of its simplicity in *phenomenologically* describing the thermal continuum.

[4] This feature was previously associated (Tomsick, Corbel & Kaaret 2001) with the emission from the Galactic ridge (Valinia & Marshall 1998).

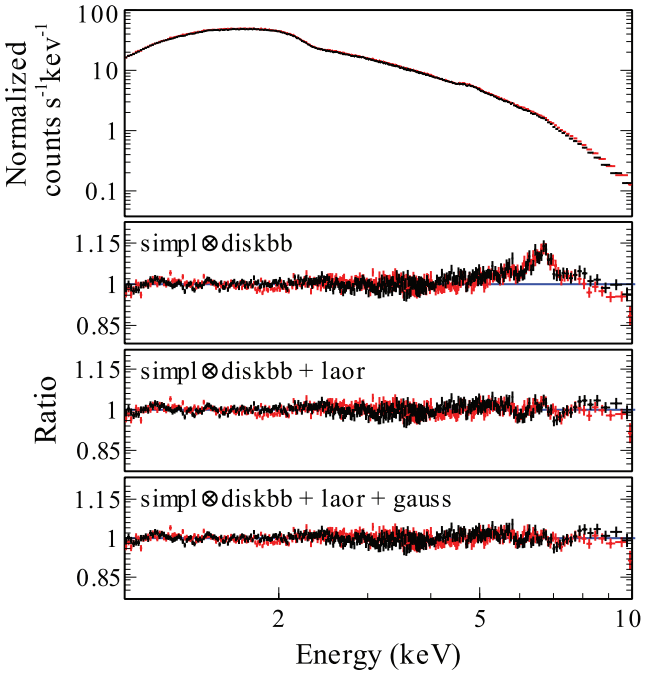

Figure 8. Top panel: the *ASCA* spectra. Below are plots of the ratio of the data to a phenomenological continuum model consisting of thermal-disc and Compton components plus a LAOR line; in the bottommost panel, a narrow Gaussian line has been added to the model.

are usually present at ≈7.1 keV in TD-state spectra of BH binaries (Done et al. 1992; Reis et al. 2008). In order to properly account for the panorama of features associated with the reprocessing of radiation in the accretion disc, we now consider complete reflection models.

6.2 Reflection analysis – *ASCA*

We replace the LAOR component with REFLIONX (Ross & Fabian 2005), which describes the spectrum reflected from an optically-thick and cold atmosphere of constant density that is illuminated by a power-law spectrum (Section 4). The parameters of the model are the iron abundance (set to solar), photon index of the illuminating power law, ionization parameter and normalization. The gravitational and Doppler effects are accounted for using the fully relativistic convolution model KERRCONV (Brenneman & Reynolds 2006), which includes BH spin as a fit parameter. The power-law indices of REFLIONX and the Compton component (SIMPL-R) are tied and, as before, we constrain the inclination to lie between 71° and 78° and include a narrow Gaussian line at ≈6.7 keV. The model results in a good and improved fit to the data with $\chi^2/\nu = 1752.3/1499$ (Model 2 in Table 4); however, it still does not fully account for the reflection features, with residuals present at ≈7 keV (top panel of Fig. 9).

Although the scattered fraction for this spectrum is high, $f_{\rm SC} > 50$ per cent, and the CF method is not applicable, we nevertheless investigated the effect of switching the continuum model from DISKBB to KERRBB (Model 3), with the mass, distance and inclination frozen at their nominal values. This change produced insignificant differences in the fit parameters (Table 4). For both Models 2 and 3, we find that the spin parameter is moderate (<0.75). Meanwhile, the disc ionization has pegged at its maximum value ($\xi = 10^4$ erg cm^{-2} s^{-1}) indicating that the surface layer of the

Table 4. *ASCA* 1–10 keV spectral fit parameters with a variety of reflection-based models.

Parameters	Model 1	Model 2	Model 3	Model 4	Model 5
	SIMPL⊗DISKBB +LAOR	SIMPL-R⊗DISKBB +KERRCONV⊗REFLIONX	SIMPL-R⊗KERRBB +KERRCONV⊗REFLIONX	POWERLAW +KERRCONV⊗REFBHB	
$N_{\rm H}$ ($\times 10^{22}$ cm^{-2})	$0.576^{+0.003}_{-0.002}$	$0.650^{+0.006}_{-0.002}$	$0.666^{+0.002}_{-0.007}$	$0.663^{+0.002}_{-0.006}$	$0.653^{+0.009}_{-0.007}$
Γ	2.40 ± 0.01	$2.329^{+0.006}_{-0.010}$	$2.320^{+0.003}_{-0.002}$	2.24 ± 0.01	$2.22^{+0.03}_{-0.02}$
$f_{\rm SC}$ ($N_{\rm hard}$)[a]	0.6 ± 0.3	0.64 ± 0.04	0.616 ± 0.002	2.4 ± 0.1	$2.3^{+0.2}_{-0.1}$
kT (keV)	$0.513^{+0.009}_{-0.006}$	$0.566^{+0.001}_{-0.013}$	–	0.540 ± 0.001	$0.542^{+0.002}_{-0.001}$
$N_{\rm diskbb}$ $[(\frac{R/{\rm km}}{D/10\,{\rm kpc}})^2 \cos i]$	5200^{+500}_{-200}	4211^{+86}_{-272}	–	–	–
$\dot{M}$ ($\times 10^{18}$ gs^{-1})	–	–	$0.668^{+0.003}_{-0.03}$	–	–
q	2.0 ± 0.2	1.88 ± 0.01	$1.85^{+0.2}_{-0.30}$	$2.38^{+0.04}_{-0.07}$	$2.5^{+0.2}_{-0.1}$
i (°)	71–78	71–78	71–78	77 ± 1	82_{-3}
$E_{\rm Laor}$ (keV)	$6.40^{+0.01}$	–	–	–	–
$r_{\rm in}$ ($r_{\rm g}$)	$8.2^{+2.9}_{-3.5}$	–	–	–	–
$N_{\rm Laor}$ ($\times 10^{-3}$)	7.1 ± 0.1	–	–	–	–
ξ (erg cm s^{-1})	–	$10\,000_{-320}$	$10\,000_{-900}$	–	–
$N_{\rm reflionx}$ ($\times 10^{-6}$)	–	1.32 ± 0.06	$1.288^{+0.004}_{-0.070}$	–	–
$H_{\rm den}$ ($\times 10^{22}$ H cm^{-3})	–	–	–	$1.00_{-0.02}$	$1.00_{-0.02}$
$F_{\rm illum}/F_{\rm bb}$	–	–	–	$0.29^{+0.03}_{-0.18}$	$0.25^{+0.08}_{-0.07}$
$N_{\rm refbhb}$ ($\times 10^{-2}$)	–	–	–	$6.2^{+0.2}_{-2.7}$	$5.96^{+0.5}_{-1.1}$
Spin (a_*)	–	<0.75	0.45(<0.75)	0.6(>0.38)	$0.55^{+0.15}_{-0.22}$
χ^2/ν	1848.0/1501	1752.3/1499	1759.5/1499	1700.9/1498	1698.6/1498

Notes. All errors are quoted at the 90 per cent confidence level for one parameter of interest ($\Delta\chi^2 = 2.71$). Model 1, which is purely phenomenological, uses the familiar LAOR line and allows a comparison with previous work. Models 2 and 3 use different disc components; however, both of them employ the same full reflection model (REFLIONX), while treating the Compton component using SIMPL-R (Section 4.1). The core of Model 4 is REFBHB which is likewise a full reflection model, with the added virtue that it self-consistently models the thermal component as well. In Models 1–4, the inclination was constrained to be between 71° and 78°. In Model 5, the inclination is allowed to range from 60° to 82°. A constraint on the inclination was achieved only for Models 4 and 5.

[a]The POWERLAW normalization is in photon cm^{-2} s^{-1} for Models 4 and 5. For Models 1–3, the normalization is given by the dimensionless parameter $f_{\rm SC}$ (see Section 3).

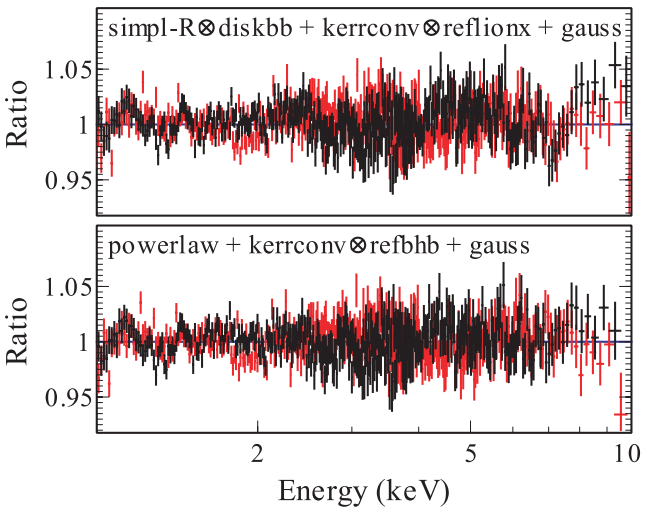

Figure 9. Data-to-model ratio for (top panel) the REFLIONX model together with a separate thermal emission and a Compton component. Bottom panel: self-consistent thermal emission and reflection (REFBHB) together with a power-law component.

accretion disc is highly ionized, with iron possibly being fully ionized. In such circumstances, the Fe absorption edge can be particularly strong and is often found to be highly smeared (see Ross et al. 1996, and references therein).

In order to incorporate the effects of thermal ionization expected for a hot accretion disc, we replace REFLIONX with the model REFBHB developed by Ross & Fabian (2007). This reflection model accounts for both thermal X-ray emission and the reflection features. The effects of Compton broadening in the disc are fully included, subject to the one assumption of a constant-density atmosphere. The parameters of the model are the number density of hydrogen in the illuminated surface layer, $H_{\rm den}$, the temperature of the blackbody heating the surface layers, the power-law photon index, and the ratio of the total flux illuminating the disc to the total blackbody flux emitted by the disc. Again, we tie the power-law index of REFBHB to that of the Compton component – now modelled as a standard power law – and convolve the spectrum with KERRCONV in order to include relativistic broadening. The model results in an excellent fit to the data with $\chi^2/\nu = 1700.9/1498$ (Model 4, see the bottom panel in Fig. 9); however, the hydrogen surface density is pegged at the maximum value of the model. The ionization state of the disc is inversely proportional to the value of the hydrogen density and thus the pegged value implies that the fit is requiring a higher amount of emission in the form of discrete features as opposed to the near-featureless reflected continuum arising from a highly ionized disc surface. A similar result would be produced by increasing the iron abundance. Unfortunately, the model in its current format does not allow for a change in elemental abundances. In order to investigate the effect that $H_{\rm den}$ has on the spin parameter, we fixed it at 1×10^{21} H cm^{-3} using Model 4 (i.e. an order of magnitude less than the value presented in Table 4) and refitted the data. This constraint on $H_{\rm den}$ resulted in an adequate fit with $\chi^2/\nu = 1731.6/1499$ and a spin value of 0.60 ± 0.05. We note here that POWERLAW has been used to model the Compton component. We have explored replacing POWERLAW with SIMPL-R, and the fit becomes worse with

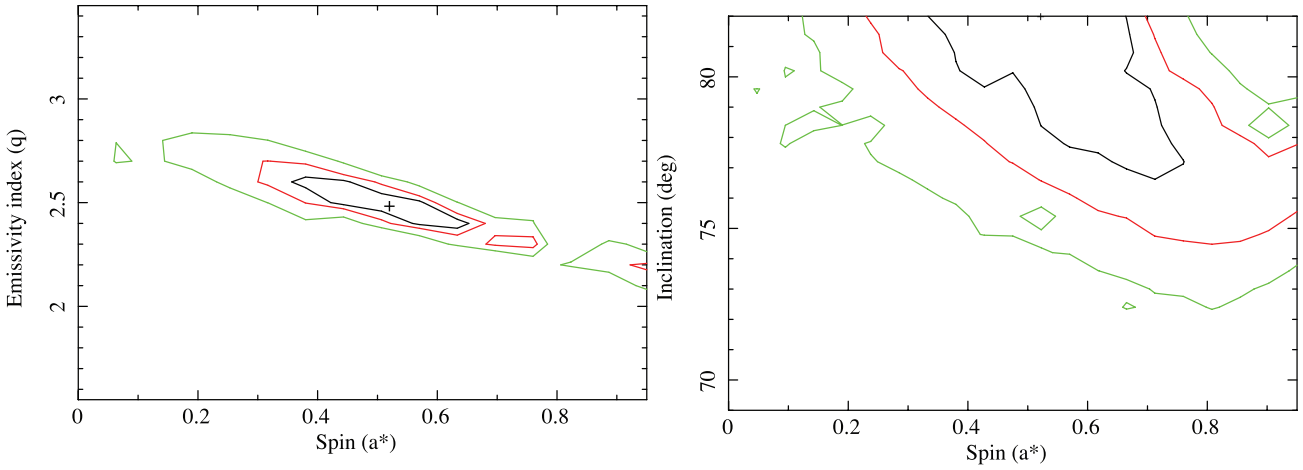

Figure 10. Left-hand panel: emissivity versus spin contour plot for J1550. The 68, 90 and 95 per cent confidence ranges for two parameters of interest are shown in black, red and green, respectively. We have allowed i to take any value between $60 \leqslant i \leqslant 82$ and found that the spin is greater than 0.33 at the 90 per cent level of confidence. Right-hand panel: a similar plot for inclination versus spin. We see from the *ASCA* data that a zero spin value is clearly ruled out, as is an inclination lower than 72°.

$\chi^2/\nu = 1802.5/1498$. However, the value of the spin parameter, as well as those of the reflection parameters, remains largely unchanged.

From Models 1 to 4, it is clear that the spin parameter is consistently below ≈0.75. However, in the first three cases, the inclination is not constrained. For this reason, we explore a very broad range of i, from 60° to 82°. We note that above this limit, the disc would be super-Eddington during its steady thermal plateau in Fig. 1. The best fit is given by Model 5 (Table 4) and reaches the upper inclination limit, netting a small improvement ($\Delta\chi^2 = -2.3$) over Model 4. For all models, we see that the emissivity index is consistently below the typical value of 3 associated with the canonical 'lamp-post' coronal geometry and is instead more consistent with a slab-like corona. In order to illuminate any degeneracy between the value of spin and either the emissivity index or the inclination, we show in Fig. 10 the 68, 90 and 95 per cent probability contours for these parameters plotted versus spin. In both instances, there exists a small and negative correlation with spin. However, it is also clear that q is well constrained between 2.2 and 2.7 and that $i \gtrsim 75°$ at 90 per cent confidence even while including the uncertainty in spin. When we marginalize over these parameters for Model 5 and compute the uncertainty in spin alone (Fig. 11), the spin parameter obtained from the gravitational blurring of reflection features is constrained to be in the window $0.33 < a_* < 0.70$ at 90 per cent confidence with the best estimate at $a_* \approx 0.55$. A non-rotating Schwarzschild BH is rejected at greater than 3σ.

Our measured spin from Fe Kα using the REFBHB model is consistently lower than the preliminary value of $a_* = 0.75$–0.80 reported by Miller et al. (2009b), and we have attained a better fit than they have obtained ($\Delta\chi^2 \lesssim -100$) for more degrees of freedom. The critical difference in our model and spin estimate comes from having incorporated the effect Compton-broadening of the Fe Kα line in the hot layers of the accretion disc. With REFBHB the disc is intrinsically hot and therefore the effect of Compton-broadening is fully accounted for when modelling the data. The extra broadening caused by this effect acts to lower the degree of gravitational broadening and as such requires less extreme spin parameters as compared to models where the reflection is assumed to come from a relatively cold surface, for example, for AGNs (Ross & Fabian 2007). Generically, it is thus expected that REFLIONX (designed specifically for cold discs) should estimate faster spin values than REFBHB. The effect is moderate, but still evident when comparing the upper limits on spin from Table 4 in which we see that the 90 per cent upper bound extends to 0.75 for Models 2 and 3 (using REFLIONX) as compared to 0.7 for Model 5, which uses REFBHB.

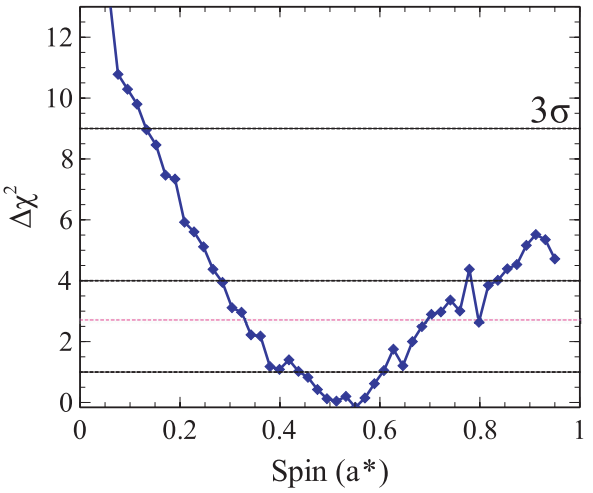

Figure 11. Goodness-of-fit versus spin parameter for J1550. From the reflection features present in the *ASCA* spectra of J1550, we can rule out a non-rotating BH at over 3σ confidence. However, we cannot place a comparable strong upper limit on this value. The 90 per cent confidence level ($\Delta\chi^2 = 2.71$ for one parameter of interest) is shown in magenta. The black dotted lines indicate confidence intervals. The spin is constrained to $0.33 < a_* < 0.70$ at the 90 per cent confidence level.

6.3 Spin from reflection features – *RXTE*

In order to supplement the *ASCA* spin measurement above, we present an analysis of a sample of 10 *RXTE* spectra selected from the composite data set discussed in Sections 3 and 4 to have the following properties: very large scattered fraction, $f_{\rm SC} > 50$ per cent, goodness of fit, $\chi^2/\nu < 2$, and uniform values of the luminosity and photon index, $L_{\rm D}/L_{\rm Edd} \approx 0.2 \pm 0.05$ and $\Gamma \approx 2.5 \pm 0.1$, respectively. We begin by simultaneously modelling the reflection features

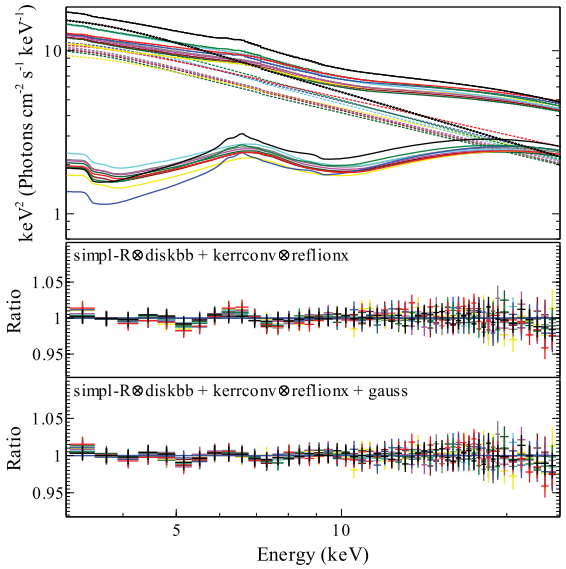

Figure 12. Best-fitting model (top panel) for the 10 *RXTE* observations. The model consists of a disc and a Compton continuum together with a relativistically blurred reflection component. The spin, inclination and emissivity index were treated as global parameters (see Section 6.3). Middle panel: data-to-model ratio for the above model. Bottom panel: data-to-model ratio for the above model after the inclusion of a narrow Gaussian emission line.

present in all the *RXTE* spectra using REFLIONX convolved with KERRCONV while using SIMPL-R⊗DISKBB for the thermal plus Compton continuum (Model 2 in Section 6.2). (NB: The REFBHB component used in Models 4 and 5 was unable to converge to an adequate fit for the *RXTE* spectra and provided no spin constraint. Therefore, in this section, we adopt Model 2.) The spin, inclination ($60 \leqslant i \leqslant 82$) and emissivity index[5] are treated as global parameters among the 10 spectra. As in Section 3, the neutral hydrogen column density was fixed at 8×10^{21} cm^{-2}. The remaining parameters were allowed to vary in individual spectra. Fig. 12 shows the best-fitting model spectra (top panel) together with the data-to-model ratio for each spectrum (bottom panel). The fit was marginally improved ($\Delta\chi^2 = -30.5$ for 10 degrees of freedom) by including a narrow line at $\approx$6.7 keV which accounts for the slight curvature in the residuals at that energy (compare the two lower panels in Fig. 12).

We find that the global best fit is sensitive to the upper energy range adopted for the *RXTE* spectra, which we attribute in part to a competition between the lower energy reflection features and the high-energy Compton hump. Considering an upper range 12–45 keV, the best spin estimate was found in the range $a_* \approx 0.6$–0.69, giving reduced χ^2 values from $\chi^2/\nu = 0.4$ to 0.8, with higher values obtained at extended energy ranges. Most importantly, the model consistently estimated the 90 per cent upper limit for spin at $a_* = 0.75$. For the other global parameters, we treat the *RXTE* results as second tier, but find results consistent with the *ASCA* values: $q \approx 2.5$ and $i > 72^\circ$ (90 per cent).

We are cautious in interpreting this spin estimate using *RXTE* spectral fits, owing to the coarse ($\sim$20 per cent) energy resolution. However, we expect that the *RXTE* should provide robust upper bounds on the degree of relativistic broadening (viz. spin), owing to its vast collecting area and $\lesssim$1 per cent spectral calibration (Jahoda et al. 2006). We caution towards the significance of the *RXTE*-derived spin parameter and consider the upper limit obtained here as a *complementary result* to that obtained from the *ASCA* data alone, confirming that the Fe Kα spin is not high.

[5] Because we have selected a homogeneous set of spectra with almost identical luminosities, it is likely that the emissivity index – an indicator of coronal geometry – is the same for all 10 spectra.

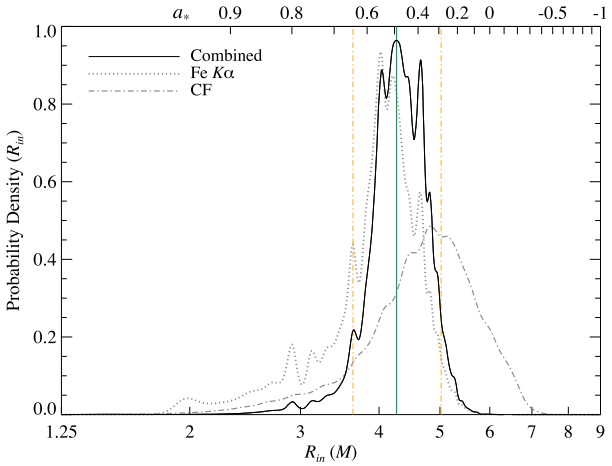

Figure 13. Combined Fe Kα and CF probability density for $R_{\rm in}$ and a_*. The net result is again a moderate value in between the two individual estimates ($a_* = 0.49^{+0.13}_{-0.20}$, 90 per cent confidence).

7 DISCUSSION

7.1 A combined Fe Kα and CF result

In the previous two sections, we concluded that both the Fe Kα line and CF methods predict moderate values of spin, which are quite consistent: $0.33 < a_* < 0.70$ (*ASCA* only) and $-0.11 < a_* < 0.71$, respectively (90 per cent confidence). The CF spin result predicts a slightly narrower Fe-line feature than that found by the Fe-line analysis. Alternatively, the Fe-line measurements consistently favour a high inclination and therefore require a lesser distance ($D \approx 4$ kpc), in order for the CF results to match.

Having obtained two independent measurements of the spin, we now combine them by convolving the individual spin probability distributions to obtain the joint distribution shown in Fig. 13. Our synthesized result is then $0.29 < a_* < 0.62$, with a most probable value of $a_* = 0.49$. Remarkably, based on a model of binary evolution and the GRB collapsar model, Brown, Lee, Moreno Méndez (2007) predicted that J1550 formed with $a_* \approx 0.5$. Our results are consistent with their prediction.

7.2 Testing the no-hair theorem

The no-hair theorem states that a macroscopic BH is described by just two parameters: M and a_*.[6] A violation of the no-hair theorem would prove that either the object in question is not a bona fide Kerr BH or general relativity is in error. Presently, tests of the no-hair theorem proposed by various groups centre on searching for deviations of the quadrupole and higher moments from the expected Kerr value (see e.g. Ryan 1997; Will 2008; Johannsen & Psaltis 2010; Vigeland & Hughes 2010; Bambi & Barausse 2011).

[6] In principle, it could have an electric charge, but astrophysical BHs are unlikely to have enough charge to be dynamically important.

The Fe-line and CF methods both rely upon a common assumption that $R_{\rm ISCO}$ is the truncation radius of the disc. However, under alternative theories of gravity, one expects the two methods to deliver different values of spin because the models will scale differently with radius. This measured discrepancy could then be rectified by appealing to perturbations to the Kerr solution (akin to those described by the works mentioned above). The fact that we find consistent values of spin provides tacit support for the no-hair theorem. However, the errors in both spin measurements are large, and we do not yet understand all sources of systematic error. Nevertheless, this example gives a foretaste of how spin measurements can contribute to deep questions in physics.

7.3 Confronting GRMHD simulations

Recently, it has become feasible, via GRMHD simulations, to assess the differences between magnetorotational instability driven accretion flows and the idealized α-disc model, upon which our CF model is based. Differences include both a non-zero torque inside the ISCO and an altered angular momentum profile for the disc.

To calibrate the magnitude of these differences in the context of the CF model, Kulkarni et al. (2011) have analysed a suite of GRMHD simulations of the accretion on to spinning BHs. Because it is computationally very expensive to simulate thin discs, the discs they consider are about twice as thick as those considered in this paper. In general, they conclude that deviations from the Novikov–Thorne model, upon which the CF method is based, tend to overestimate spin ($r_{\rm in}$ is too small by several per cent and deviates more for thicker discs and at higher inclinations). For the inclination of J1550, they find that the magnitude of this bias is $\approx$10 per cent ($\Delta a_* \approx 0.13$). We note that the actual change is expected to be smaller over the luminosity range we use because the discs we consider are significantly thinner.

Similar MHD simulations have been made to assess a principal assumption of the Fe-line method, namely that the line emission from within the ISCO is negligible (Reynolds & Fabian 2008). Including the effect of contributing plunging-region emission results in intrinsically broader line profiles and hence will lower the estimate for spin. For the disc thickness and spin values in question, simulations predict that this effect could possibly shift $r_{\rm in}$ by $\sim$12 per cent (value taken from fig. 5 in Reynolds & Fabian 2008), thereby decreasing the most probable Fe Kα estimate of spin from $a_* \approx 0.55$ to $\approx$0.4, in close agreement with the best CF value of $a_* \approx 0.34$.

Based on the work of Kulkarni et al. (2011) and Reynolds & Fabian (2008), we conclude that both spin estimates are likely too high ($\approx$10 per cent low in $r_{\rm in}$), which strengthens our conclusion that the spin of J1550 is moderate.

7.4 The question of alignment

The spin of an accreting BH in a binary is expected to align with the orbital angular momentum vector of the system within $\approx 10^7$–10^8 yr (Maccarone 2002). A recent population synthesis study (Fragos et al. 2010), which makes conservative assumptions concerning the torques acting to align a BH, predicts that most BHs will be aligned to better than 10°. In Section 6, we constrained the inclination of the inner, reflecting portion of the accretion disc (Fig. 10). This allows us to check on the relative alignment of the BH spin axis (which is aligned with this inner disc region; Lodato & Pringle 2006) and the orbital vector. In our exploration of the Fe Kα model, for a wide range of orbital inclinations (60°–82°), we find a best-fitting inclination for the inner disc of $\approx$75°–82°. This value is consistent with the orbital inclination angle given by our dynamical model, $i = 74\overset{\circ}{.}7 \pm 3\overset{\circ}{.}8$ (Orosz et al. 2011), which validates the CF assumption of alignment (Li et al. 2005), while simultaneously providing support for the dynamical model.

7.5 Implications of a low-spin microquasar

The low spin values of J1550 and the microquasar A0620−00 ($a_* \approx 0.1$; Gou et al. 2010) challenge the long-standing and widely held belief that there is a strong connection between BH spin and relativistic jets (BZ), while these low spin values support the conclusion of a literature study by Fender, Gallo & Russell (2010) that found no evidence for a correlation between BH spin and jet power. By contrast, simulations strongly suggest that if jets are powered by BH spin, then the jet power will increase dramatically with increasing a_* (Tchekhovskoy et al. 2010). However, it is alternatively possible for a magnetized disc to directly power a jet (here, a centrifugally driven outflow) without any need to harness power from the spin of the BH (Blandford & Payne 1982; hereinafter BP). In fact, more power can potentially be provided to a jet by the disc under the BP mechanism than from the BH's spin (via the BZ mechanism) for spin values $a_* < 0.4$. For these discs, the rotation rate at the ISCO is faster than the rotation of the BH at its horizon, and the available power from the BZ mechanism is generally low (e.g. McKinney 2005).

Given the low spin values of J1550 and A0620−00, we suggest that their episodic jets are driven in part by the accretion disc, while the jet of an extreme-spin source like GRS 1915+105 (McClintock et al. 2006; Blum et al. 2009) may instead be fully powered by the BZ mechanism. A useful comparison of the operational regimes of BP and BZ is given by Garofalo et al. (2010). They show that BP is always viable, but that BZ is the more likely mechanism for high-spin sources to produce jets. We note the caveat that there is no definitive measurement of J1550's jet power and that the magnetic field of the disc is likewise difficult to estimate; our claim is motivated purely by the existence of powerful jets in two low-spin microquasars.

The relativistic, two-sided jet of J1550 was launched during the remarkable 7-Crab flare (see Section 1). In what follows, we show that during this day-long event, the luminosity of the accretion disc was close to, or perhaps at, its Eddington limit. The synchronicity of this extreme-luminosity condition of the disc and the jet-launching X-ray flare suggest that radiation pressure may have been important in collimating or feeding the jet (possibly indirectly via a radiatively driven disc wind; for a discussion of the interplay between the jet and wind, see Neilsen & Lee 2009 and Miller et al. 2008).

In Fig. 14, we plot the intrinsic accretion-disc luminosity during the flare state versus the luminosity during the thermal-dominant plateau state (days 105–182; see Fig. 1). Each data point represents an analysis of the complete J1550 data set for one triplet of values of M, i and D from among the 42 500 triplets used in our Odyssey cluster analysis (Appendix A.4). The spin value for each point (averaged over the *gold* and *silver* data) is colour-coded according to the bar at the top of the plot. The point corresponding to the dynamical model adopted from Orosz et al. (2011), their Model F, is labelled and marked by a red cross. The five less probable models considered by Orosz et al. are marked by the black crosses. We conclude that the disc in Model F (by far the most probable model; see Appendix A.5) is very near its Eddington limit at the time the jet is launched.

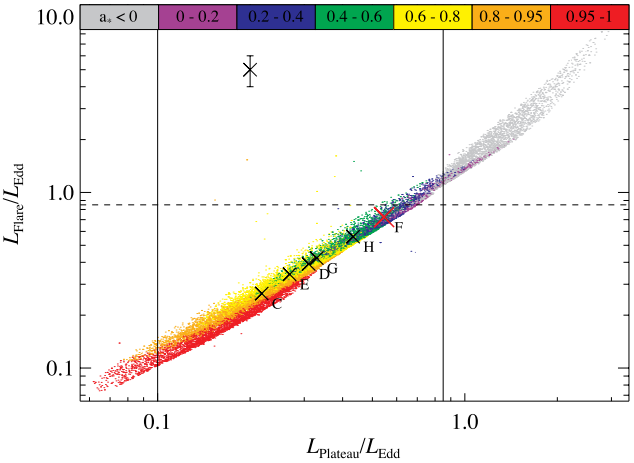

Figure 14. The intrinsic (i.e. seed) luminosity of the disc component during the 7-Crab flare versus the luminosity during the thermal plateau phase. In order to avoid saturating the plot, we show only half the data points, which were selected at random. The vertical black lines mark the lower and upper luminosity thresholds, and the horizontal dashed line corresponds to the Eddington limit of an accretion disc (Section 5). Note that Model F is very near this limit.

Luminous discs are geometrically thick and widely believed to be effective at driving jets. In the case of the J1550 flare, the disc is not only thick, but also near its Eddington limit, so that it will provide substantial radiation pressure, can sustain stronger magnetic fields and possibly shed material via a radiation-driven outflow, thereby promoting the ejection of a jet. In any case, as a bottom line, the low spin values of J1550 and A0620−00 indicate that spin is not the sole driver behind all powerful episodic jets.

8 CONCLUSIONS

For the first time in a single work, we have determined high-quality, independent estimates of the spin of an accreting BH using the two leading methods. In our CF analysis, we carefully explored the sensitivity of our results to a wide range of model-dependent systematic errors and observational errors. We conclude that J1550 is a slowly spinning BH with $a_* \approx 0.34$, while ruling out spin values larger than $a_* \gtrsim 0.71$ at 90 per cent confidence. Next, we analysed the Fe Kα and reflection signatures in bright, intermediate spectral states of J1550. By modelling these broad, skewed features, we obtained a slightly higher estimate of the spin, $a_* \approx 0.55^{+0.15}_{-0.22}$ (at 90 per cent confidence), while also deriving an estimate of the inclination angle of the inner disc that is in close agreement with the orbital inclination angle (Orosz et al. 2011). Combining the two spin estimates, we conclude that J1550, like the microquasar A0620−00, is a slowly spinning BH.

The low spin values of both J1550 and A0620−00 indicate that, for at least some microquasars, BZ-type mechanisms are not primary in driving powerful episodic jets and that other mechanisms (perhaps BP) are at play. The near-Eddington-limited 7-Crab flare observed for J1550 suggests that radiation-pressure support from a thermal disc is one possible way that low-spin BHs are aided in driving large-scale relativistic jets.

ACKNOWLEDGMENTS

JFS was supported by the Smithsonian Institution Endowment Funds and JEM acknowledges support from NASA grant NNX08AJ55G. RN acknowledges support from NASA grant NNX08AH32G and NSF grant AST-0805832. RCR would like to thank the Science and Technology Research Council and the Smithsonian Astrophysical Observatory for financial support. JFS thanks Bob Penna and Sasha Tchekhovskoy for helpful discussions, and the FAS Sciences Division Research Computing Group for their technical support with analyses performed on the Odyssey cluster.

REFERENCES

Akaike H., 1974, IEEE Trans. Autom. Control, AC-19, 716
Arnaud K. A., 1996, in Jacoby G. H., Barnes J., eds, ASP Conf. Ser. Vol. 101, Astronomical Data Analysis Software and Systems V. Astron. Soc. Pac., San Francisco, p. 17
Arvanitaki A., Dimopoulos S., Dubovsky S., Kaloper N., March-Russell J., 2010, Phys. Rev. D, 81, 123530
Bambi C., Barausse E., 2011, ApJ, 731, 121
Beloborodov A. M., 1999, ApJ, 510, L123
Berti E., Volonteri M., 2008, ApJ, 684, 822
Blandford R. D., Payne D. G., 1982, MNRAS, 199, 883 (BP)
Blandford R. D., Znajek R. L., 1977, MNRAS, 179, 433 (BZ)
Blum J. L., Miller J. M., Fabian A. C., Miller M. C., Homan J., van der Klis M., Cackett E. M., Reis R. C., 2009, ApJ, 706, 60
Brenneman L. W., Reynolds C. S., 2006, ApJ, 652, 1028
Brown G. E., Lee C., Moreno Méndez E., 2007, ApJ, 671, L41
Burnham K. P., Anderson D. R., 2002, Model Selection and Multimodel Inference. Springer-Verlag, New York
Campanelli M., Lousto C. O., Zlochower Y., 2006, Phys. Rev. D, 74, 041501
Corbel S. et al., 2001, ApJ, 554, 43
Corbel S., Fender R. P., Tzioumis A. K., Tomsick J. A., Orosz J. A., Miller J. M., Wijnands R., Kaaret P., 2002, Sci, 298, 196
Davis S. W., Hubeny I., 2006, ApJS, 164, 530
Davis S. W., Blaes O. M., Hubeny I., Turner N. J., 2005, ApJ, 621, 372
Davis S. W., Done C., Blaes O. M., 2006, ApJ, 647, 525
Done C., Mulchaey J. S., Mushotzky R. F., Arnaud K. A., 1992, ApJ, 395, 275
Done C., Gierliński M., Kubota A., 2007, A&AR, 15, 1
Dunn R. J. H., Fender R. P., Körding E. G., Belloni T., Cabanac C., 2010, MNRAS, 403, 61
Ebisawa K., 1999, in Poutanen J., Svensson R., eds, ASP Conf. Ser. Vol. 161, High Energy Processes in Accreting Black Holes. Astron. Soc. Pac., San Francisco, p. 39
Ebisawa K. et al., 1994, PASJ, 46, 375
Esin A. A., McClintock J. E., Narayan R., 1997, ApJ, 489, 865
Fabian A. C., Rees M. J., Stella L., White N. E., 1989, MNRAS, 238, 729
Fabian A. C. et al., 2009, Nat, 459, 540
Fender R. P., Gallo E., Russell D., 2010, MNRAS, 406, 1425
Fragos T., Tremmel M., Rantsiou E., Belczynski K., 2010, ApJ, 719, L79
García J., Kallman T. R., 2010, ApJ, 718, 695
Garofalo D., Evans D. A., Sambruna R. M., 2010, MNRAS, 406, 975
Gierliński M., Done C., 2003, MNRAS, 342, 1083
Gou L. J. et al., 2009, ApJ, 701, 1076
Gou L., McClintock J. E., Steiner J. F., Narayan R., Cantrell A. G., Bailyn C. D., Orosz J. A., 2010, ApJ, 718, L122
Hannikainen D. C. et al., 2009, MNRAS, 397, 569
Homan J., Wijnands R., van der Klis M., Belloni T., van Paradijs J., Klein-Wot M., Fender R., Méndez M., 2001, ApJS, 132, 377
Hurvich C. M., Tsai C.-L., 1989, Biometrika, 76, 297
Jahoda K., Markwardt C. B., Radeva Y., Rots A. H., Stark M. J., Swank J. H., Strohmayer T. E., Zhang W., 2006, ApJS, 163, 401
Johannsen T., Psaltis D., 2010, ApJ, 716, 187
Kaaret P., Corbel S., Tomsick J. A., Fender R., Miller J. M., Orosz J. A., Tzioumis A. K., Winjands R., 2003, ApJ, 582, 945
King A. R., Pringle J. E., Livio M., 2007, MNRAS, 376, 1740
Kubota A., Done C., 2004, MNRAS, 353, 980
Kulkarni A. K. et al., 2011, MNRAS, in press
Laor A., 1991, ApJ, 376, 90

Lee C., Brown G. E., Wijers R. A. M. J., 2002, ApJ, 575, 996
Li L.-X., Zimmerman E. R., Narayan R., McClintock J. E., 2005, ApJS, 157, 335
Liu J., McClintock J. E., Narayan R., Davis S. W., Orosz J. A., 2008, ApJ, 679, L37
Liu J., McClintock J. E., Narayan R., Davis S. W., Orosz J. A., 2010, ApJ, 719, L109
Lodato G., Pringle J. E., 2006, MNRAS, 368, 1196
Maccarone T. J., 2002, MNRAS, 336, 1371
McClintock J. E., Shafee R., Narayan R., Remillard R. A., Davis S. W., Li L.-X., 2006, ApJ, 652, 518
McClintock J. E., Remillard R. A., Rupen M. P., Torres M. A. P., Steeghs D., Levine A. M., Orosz J. A., 2009, ApJ, 698, 1398
McKinney J. C., 2005, ApJ, 630, L5
McNamara B. R., Kazemzadeh F., Rafferty D. A., Bírzan L., Nulsen P. E. J., Kirkpatrick C. C., Wise M. W., 2009, ApJ, 698, 594
Magdziarz P., Zdziarski A. A., 1995, MNRAS, 273, 837
Miller J. M., 2007, ARA&A, 45, 441
Miller J. M. et al., 2001, ApJ, 563, 928
Miller J. M. et al., 2003, MNRAS, 338, 7
Miller J. M., Fabian A. C., Nowak M. A., Lewin W. H. G., 2005, in Novello M., Perez Bergliaffa S., Ruffini R., eds, On Recent Developments in Theoretical and Experimental General Relativity, Gravitation and Relativistic Field Theories. World Scientific Press, Singapore, p. 1296
Miller J. M., Raymond J., Reynolds C. S., Fabian A. C., Kallman T. R., Homan J., 2008, ApJ, 680, 1359
Miller J. M., Cackett E. M., Reis R. C., 2009a, ApJ, 707, L77
Miller J. M., Reynolds C. S., Fabian A. C., Miniutti G., Gallo L. C., 2009b, ApJ, 697, 900
Miniutti G., Panessa F., de Rosa A., Fabian A. C., Malizia A., Molina M., Miller J. M., Vaughan S., 2009, MNRAS, 398, 255
Mirabel I. F., Rodríguez L. F., 1999, ARA&A, 37, 409
Mitsuda K. et al., 1984, PASJ, 36, 741
Narayan R., McClintock J. E., 2005, ApJ, 623, 1017
Neilsen J., Lee J. C., 2009, Nat, 458, 481
Noble S. C., Krolik J. H., Hawley J. F., 2009, ApJ, 692, 411
Noble S. C., Krolik J. H., Hawley J. F., 2010, ApJ, 711, 959
Novikov I. D., Thorne K. S., 1973, Black Holes (Les Astres Occlus). Gordon and Breach, Paris
Orosz J. A. et al., 2002, ApJ, 568, 845
Orosz J. A., Steiner J. F., McClintock J. E., Torres M. A. P., Remillard R. A., Bailyn C. D., Miller J. M., 2011, ApJ, 730, 75
Penna R. F., McKinney J. C., Narayan R., Tchekhovskoy A., Shafee R., McClintock J. E., 2010, MNRAS, 408, 752
Reis R. C., Fabian A. C., Ross R. R., Miniutti G., Miller J. M., Reynolds C., 2008, MNRAS, 387, 1489
Reis R. C., Fabian A. C., Ross R. R., Miller J. M., 2009, MNRAS, 395, 1257
Reis R. C. et al., 2011, MNRAS, 410, 2497
Remillard R. A., McClintock J. E., 2006, ARA&A, 44, 49
Remillard R. A., Muno M. P., McClintock J. E., Orosz J. A., 2002a, ApJ, 580, 1030
Remillard R. A., Sobczak G. J., Muno M. P., McClintock J. E., 2002b, ApJ, 564, 962
Reynolds C. S., Fabian A. C., 2008, ApJ, 675, 1048
Reynolds C. S., Nowak M. A., 2003, Phys. Rep., 377, 389
Ross R. R., Fabian A. C., 1993, MNRAS, 261, 74
Ross R. R., Fabian A. C., 2005, MNRAS, 358, 211
Ross R. R., Fabian A. C., 2007, MNRAS, 381, 1697
Ross R. R., Fabian A. C., Brandt W. N., 1996, MNRAS, 278, 1082
Ryan F. D., 1997, Phys. Rev. D, 56, 1845
Sądowski A., Abramowicz M., Bursa M., Kluźniak W., Lasota J., Różańska A., 2011, A&A, 527, A17
Schmoll S. et al., 2009, ApJ, 703, 2171
Shafee R., McClintock J. E., Narayan R., Davis S. W., Li L.-X., Remillard R. A., 2006, ApJ, 636, L113
Shafee R., McKinney J. C., Narayan R., Tchekhovskoy A., Gammie C. F., McClintock J. E., 2008, ApJ, 687, L25
Shapiro S. L., Teukolsky S. A., 1983, Black Holes, White Dwarfs, and Neutron Stars: The Physics of Compact Objects. Wiley, New York
Sobczak G. J., McClintock J. E., Remillard R. A., Cui W., Levine A. M., Morgan E. H., Orosz J. A., Bailyn C. D., 2000, ApJ, 544, 993
Steiner J. F., McClintock J. E., Remillard R. A., Narayan R., Gou L. J., 2009a, ApJ, 701, L83
Steiner J. F., Narayan R., McClintock J. E., Ebisawa K., 2009b, PASP, 121, 1279
Steiner J. F., McClintock J. E., Remillard R. A., Gou L., Yamada S., Narayan R., 2010, ApJ, 718, L117
Tanaka Y., Lewin W. H. G., 1995, in Lewin W. H. G., van Paradijs J., van den Heuvel E. P. J., eds, X-ray Binaries. Cambridge Univ. Press, Cambridge, p. 126
Tchekhovskoy A., Narayan R., McKinney J. C., 2010, ApJ, 711, 50
Tomsick J. A., Corbel S., Kaaret P., 2001, ApJ, 563, 229
Tomsick J. A., Corbel S., Fender R., Miller J. M., Orosz J. A., Tzioumis T., Wijnands R., Kaaret P., 2003, ApJ, 582, 933
Toor A., Seward F. D., 1974, AJ, 79, 995
Valinia A., Marshall F. E., 1998, ApJ, 505, 134
Vigeland S. J., Hughes S. A., 2010, Phys. Rev. D, 81, 024030
Volonteri M., Madau P., Quataert E., Rees M. J., 2005, ApJ, 620, 69
Weisskopf M. C., Guainazzi M., Jahoda K., Shaposhnikov N., O'Dell S. L., Zavlin V. E., Wilson-Hodge C., Elsner R. F., 2010, ApJ, 713, 912
Will C. M., 2008, ApJ, 674, L25
Wilms J., Allen A., McCray R., 2000, ApJ, 542, 914
Woosley S. E., 1993, ApJ, 405, 273
Xue Y., Wu X., Cui W., 2008, MNRAS, 384, 440
Zhang S. N., Cui W., Chen W., 1997, ApJ, 482, L155
Zoghbi A., Fabian A. C., Uttley P., Miniutti G., Gallo L. C., Reynolds C. S., Miller J. M., Ponti G., 2010, MNRAS, 401, 2419

APPENDIX A: CONTINUUM FITTING: ASSESSING THE SYSTEMATIC UNCERTAINTIES

A1 Model parameters

We consider the effect of the principal parameters listed in Table 3 on our final determination of the spin (Fig. 6) for Model S (Section 3) and Model I (Section 4). Here and below, we consider only the *gold* data. As in Sections 3 and 4, we fix M, i and D at their fiducial values (Section 1). Now, element by element, we consider the changes to the parameters and model components that are given in Table 3.

As is illustrated by Fig. 6, and shown in Table 3 (P1), decreasing the viscosity parameter by a factor of 10 from $\alpha = 0.1$ to 0.01 results in a decrease in the inner disc radius by ∼3–4 per cent. This is the largest of the 17 changes listed in Table 3, and it is dwarfed by the effects of the uncertainties in the external input parameters M, i and D (Section 5), which are analysed separately.

The column density (P2–P3) is next varied over a broad range, $N_{\rm H} = (6\text{–}10) \times 10^{21}$ cm^{-2}, which corresponds to $\gtrsim 8\sigma$ relative to the *Chandra* grating value (see Section 3.2, Miller et al. 2003). We consider this extreme range because of the discrepant results for $N_{\rm H}$ obtained using *ASCA* data (see Section 6), which we attribute to an error in the calibration of the *ASCA* detectors at low energies. As shown in Table 3, our liberal estimate of the uncertainty in $N_{\rm H}$ affects our determination of $r_{\rm in}$ by <3 per cent.

We next explore the parameters of the IREFLECT model. We test smaller covering factors of 1/2 and 1/10 by linking the covering factor in IREFLECT to (negative) '$(x - 1)$', where x is a parameter of SIMPL-R. The sign is made negative to act as a switch in the model and isolate reflection from the direct (illuminating) component. Thus, we consider two cases: $x = 1.5$ (P4) and $x = 1.1$ (P5). We next try fitting for the covering factor, allowing it to vary between 0 and 1,

while also fitting for the emissivity index, which we constrain to lie in the range $2 < q < 5$ (P6). As shown in Table 3, the effect of this exercise on $r_{\rm in}$ is small, $\sim$1 per cent. We also perform a set of fits using a fixed $q = 3$ (P7; corresponding to a standard lamp-post model); the resultant fits are on average worse by $\approx 3\sigma$, while $r_{\rm in}$ shrinks by about 3 per cent.

An even smaller effect is obtained by varying the disc temperature in Model I. First, we decrease $T_{\rm disc}$ (P8) by a factor of 5 relative to its assumed value (Section 4.2), and next we try a larger temperature of 10^7 K (P9), twice the fiducial value. We find that in the former run, the ionization parameter increases, and in the latter, it decreases, but that in both cases the effect on $r_{\rm in}$ is negligible (<0.2 per cent).

To account for the high-ionization parameter measured using Model I, we test shifting the Fe Kα line to a higher intrinsic energy of 6.8 keV (P10), a value intermediate between Kα produced by He-like Fe^{+24} and H-like Fe^{+25}. This shift in the line energy causes an $\approx$2 per cent decrease in $r_{\rm in}$.

Lastly, for Model S, we adjust the width of the SMEDGE component, $W_{\rm Edge}$, to first half (P11) and then twice (P12) its nominal value of 7 keV. This impacts $r_{\rm in}$ by <0.5 per cent.

In summary, as we found earlier in our study of LMC X−3 (Steiner et al. 2010), α is the parameter (besides M, i and D) that introduces the largest uncertainty in determining spin via the CF method.

A2 Model components

We begin by substituting BHSPEC (Davis & Hubeny 2006) for the thermal disc component in place of KERRBB2 (see section 4.2 in McClintock et al. 2006 for a discussion of these relativistic disc models). The virtue of BHSPEC relative to KERRBB2 is that it directly incorporates the effects of spectral hardening; its drawback is that it does not include returning radiation, which heats the disc. Employing BHSPEC instead, we find that $r_{\rm in}$ is increased by $\approx$1–3 per cent (M1 in Table 3).

Next, we explore the possibility that the power-law component is cut off exponentially at high energy (e.g. thermal Comptonization), while allowing the cut-off energy to vary over the range $kT_{\rm e} = 25$–200 keV. ($f_{\rm SC}$ should, in principle, be corrected to achieve photon conservation; however, we did not do so here because this correction is negligible for the *gold* spectra.) We find that the effect of a possible cut-off is small, changing $r_{\rm in}$ by $\lesssim$1.5 per cent (M2). In addition, we explore generating the power law using the double-sided version of SIMPL and SIMPL-R (in place of the upscattering-only version). The effect on $r_{\rm in}$ is $\lesssim$0.3 per cent (M3).

Lastly, we examine the effect of using one reflection model versus another. We find that both IREFLECT and REFLIONX give somewhat smaller values of $r_{\rm in}$ than SMEDGE and that the effect is small, $\lesssim$3 per cent (M4, M5).

A3 Flux

As described in Section 5, we include a liberal $\sim$10 per cent uncertainty in the absolute flux calibration. Because the luminosity of the thermal component at a given colour temperature scales proportionally to $r_{\rm in}^2$, a 10 per cent adjustment to the flux normalization introduces a $\sim$5 per cent uncertainty in $r_{\rm in}$.

A4 BH mass, inclination and distance

While analysing the X-ray spectral data, we have used the best estimates for M, i and D (Section 1) taken from Model F of table 1 in Orosz et al. (2011). In order to determine how the spin measurement depends upon uncertainties in the model of Orosz et. al., we use the Odyssey computing cluster at the Harvard University and replicate our analysis over a 3D grid of 42 500 points distributed uniformly over mass, inclination and distance. The grid spans the ranges $M = 5$–$17.5\,{\rm M}_\odot$, $i = 36^\circ$–85° and $D = 3$–7 kpc. We adopt the 3-kpc-distance bound following Hannikainen et al. (2009); the 7-kpc bound is a relativistic limit based on the proper motion of the X-ray jets (Corbel et al. 2002): $D \leq c/\sqrt{\mu_a \mu_r} \lesssim 7$ kpc (e.g. Mirabel & Rodríguez 1999). At each grid point, we compute a table of the spectral hardening factor (e.g. see Gou et al. 2010) and fit all of the available TD, SPL and INT spectra. We use Model S (Section 3.2) because it is computationally efficient and has the best performance of all three CF models considered. We perform the analysis for both values of disc viscosity: $\alpha = 0.01$ and 0.1.

We then apply our data-selection criteria, obtaining a sample of *gold* and *silver* spectra (typically 50–100) at each of the 42 500 grid points. From this we derive a spin probability distribution unique to each point. Before summing over the grid, we impose the following grid-point-selection constraints: first, the grid point's inclination must be below the eclipsing limit, $i < 82^\circ$ (see e.g. Narayan & McClintock 2005) and, secondly, as discussed in Section 5, we require that the intrinsic disc luminosity during the TD-state plateau phase (days 105–181; Fig. 1) falls in the range $0.10 < L_{\rm D}/L_{\rm Edd} < 0.85$. We combine the distributions for all satisfactory grid points, weighting each according to its location in the grid (with high weights occurring at probable values of M, i and D).

A5 Rolling together the uncertainties

We combine the systematic uncertainties discussed above in two stages. Referring to Table 3, in the first stage, we combine in quadrature the individual values in the Model S column for rows P11, P12 and M1–M5 with half the value for P2 and P3 (half because the range of variation considered for $N_{\rm H}$ is so extreme). For each of the parameters $N_{\rm H}$ and $W_{\rm Edge}$, we use the larger of the deviations given in the table. The resultant error of 4.2 per cent is combined with the 5 per cent error in $r_{\rm in}$ from flux uncertainty to give a net error of 6.5 per cent. This combined uncertainty sets the half-length for a boxcar smoothing kernel that we apply to the full spin distribution. Equally weighted distributions using both values of α are included in this step.

The resulting distribution is shown in Fig. A1. Because we have so far considered just dynamical Model F, the distribution of $r_{\rm in}$ is narrower, $-0.14 < a_* < 0.57$ (90 per cent confidence level) than our final distribution shown in Fig. 6, although the most probable value of the spin is unchanged, $a_* = 0.34$. We now go on to the second stage in combining sources of error and consider an ensemble of possible dynamical models.

The case of J1550 is unusual in that there are several candidate models which produce reasonable fits to the dynamical data, which are summarized in table 1 of Orosz et al. (2011). Above, we considered only Model F, the most probable model. We now incorporate the possibility that one of the five alternative models (Models C–E and Models G and H) is correct. Models A and B do not constrain the dynamical model satisfactorily and do not allow one to obtain a useful distance estimate, and so they are disregarded here.

As was done above for Model F, a spin ($r_{\rm in}$) probability distribution is obtained for each candidate dynamical model. For each model, including Model F, we use the total χ^2 (summed for the

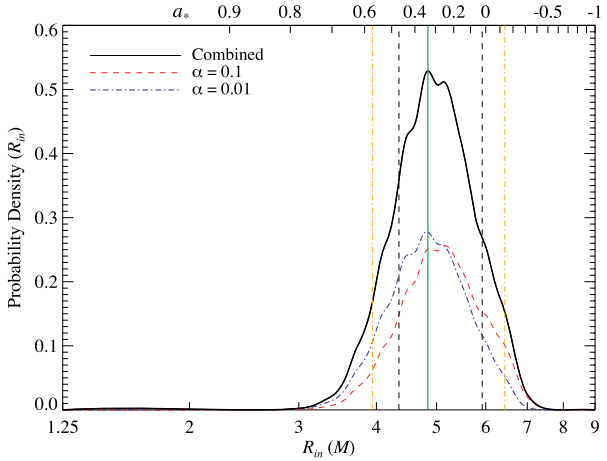

Figure A1. Similar to Fig. 6, but using just Model F in Orosz et al. (2011). The green, black and gold vertical lines indicate the most likely value for $R_{\rm in}$ (a_*), and 1σ and 90 per cent confidence interval limits, respectively.

velocity data and the light-curve data, both optical and infrared) to determine its corrected Akaike Information Criterion (AICc; Akaike 1974; Hurvich & Tsai 1989), which is closely related to the log-likelihood of each model. With these values, AIC weights are assigned to each model (i): $W_{{\rm AIC},i} = \exp[-1/2({\rm AICc}_i - \inf\{{\rm AICc}\})]$ (Burnham & Anderson 2002).

Our fiducial dynamical model is by far the most likely, carrying ∼84 per cent of the total weight. A weighted sum is computed using the AIC weights to obtain a composite spin distribution. This is broadened using the boxcar smoothing kernel described above (13 per cent width) to produce the final distribution as shown in Fig. 6. *Thus, this final result incorporates uncertainties in the choice of the dynamical model; the dynamical model uncertainties; the X-ray spectral model and parameter settings; and a 10 per cent uncertainty in the X-ray flux calibration.*

This paper has been typeset from a TEX/LATEX file prepared by the author.